The impact of peculiar velocities on the Ly-alpha forest flux power spectrum

Stoffels, Hidde

The impact of peculiar velocities on the Ly-α forest flux power spectrum

THESIS

submitted in partial fulfillment of the
requirements for the degree of

BACHELOR OF SCIENCE
in
PHYSICS & ASTRONOMY

Author :	H. Stoffels
Student ID :	s2541939
Supervisor :	A. Boyarsky
2^{nd} corrector :	M. Schaller

Leiden, The Netherlands, July 8, 2022

The impact of peculiar velocities on the Ly-α forest flux power spectrum

H. Stoffels

Huygens-Kamerlingh Onnes Laboratory, Leiden University
P.O. Box 9500, 2300 RA Leiden, The Netherlands

July 8, 2022

Abstract

Different models of dark matter can be distinguished through the amount of free streaming they exhibit. A consequence of free streaming is the suppression of small-scale cosmic structure, which in turn could be detected through the Ly-α forest, a series of absorption features in quasar spectra. This thesis considers how peculiar velocities in the intergalactic medium, the gas that produces the absorption of the Ly-α forest, influence the flux power spectrum (FPS) of the Ly-α forest. We do this by calculating the FPS from high-resolution hydrodynamical simulations, performed using the `SWIFT` code, while taking into account peculiar velocities or ignoring them; it is shown that at large scales, peculiar velocities may introduce a Gaussian cutoff to the FPS. A model that relates the spatial scale corresponding to this cutoff to the density, thermal state and peculiar velocity dispersion of the intergalactic medium is proposed and tested at redshifts $4.0 \leq z \leq 6.0$. It is found to be acceptable at $4.0 \leq z \leq 5.5$, although only the average dependence on the peculiar velocity dispersion is correctly described; at $z = 6.0$, the proposed model can be rejected. The main venue for extending the research done here is thought to be the development of a model that describes the influence of peculiar velocities on smaller scales as well.

Contents

Chapter 1

Introduction

One of the crucial components of modern cosmology is the existence of 'dark matter', a substance that – as of yet – has only been observed to interact with the baryonic component of the universe (i.e. hadrons and charged leptons) through gravity. The observations indicating the existence of dark matter are diverse:

- The rotational speeds of spiral galaxies and the velocity dispersions of dwarf galaxies exceed the predictions based on their visible matter distributions [1, 2].
- The X-ray emission from intergalactic gas in clusters suggests that the source of gravity that is responsible for establishing hydrostatic equilibrium is much stronger than can be inferred from visible gas [3].
- Gravitational lensing by galaxies is much stronger than expected based on their visible contents [4].
- If galaxies grew from the density concentrations that produced the anisotropy in the cosmic microwave background, there would not have been enough time to produce the galaxies we see today (see the end of section 2.3.2).

To explain these discrepancies between the visible mass and the mass inferred on the basis of gravitational effects, a plethora of models have been proposed, ranging from primordial black holes [5] to sterile neutrinos [6, 7] and modifications to gravity [8]. However, observations like the Bullet Cluster, in which the matter distribution as mapped through gravitational lensing is significantly displaced from the baryonic distribution as traced by X-ray emission [9] pose a significant problem to modified gravity. A combination of observations also virtually excludes compact objects such as primordial black holes as explanation [10]. Because of this, most current work focuses on explaining these observations as being due to dark matter in the form of a new particle, an extension to the Standard Model of particle physics. Such dark matter is currently estimated to constitute some 80% of the matter contents of the universe (the rest being baryonic), or a quarter of the total energy contents (with baryons constituting some 5% and dark energy the remainder) [11].
However, the Standard Model can be extended in many ways, and a bewildering variety of models have been proposed. Empirically constraining any property of dark matter particles – e.g. their mass, interaction strength, spin et cetera – could help in

distinguishing between these models; one such property is the 'free-streaming length'. Free streaming is a phenomenon that arises in the large scale structure (LSS) of the universe because relativistic particles cannot be bound gravitationally[1], which means that they can diffuse out of density concentrations, thereby erasing inhomogeneity. The scale on which the dark matter density field is smoothed by free streaming is called the free-streaming length λ_{fs}; it is set by the initial velocity distribution of the dark matter particles and the subsequent evolution of this distribution [12]. Measuring λ_{fs} would thus constrain the initial velocity distribution of dark matter.
The free-streaming length has interesting consequences for the LSS, which arises through the growth of small initial perturbations in the density field [13]. As free streaming erases inhomogeneity, structures in the LSS on scales smaller than λ_{fs} will be suppressed, which allows us to classify dark matter candidates into three general classes:

1. Cold dark matter (CDM) has a negligible λ_{fs} and thus allows structures to form on practically all scales. Since CDM does not exhibit significant free streaming, its constituent particles never move at relativistic speeds.

2. Warm dark matter (WDM) has small but cosmologically relevant λ_{fs} (i.e. smaller than or roughly at galactic scales [12]). In general, WDM particles move relativistically until some time well before the end of the radiation epoch.

3. Hot dark matter (HDM) has large λ_{fs} (i.e. larger than galactic scales). HDM would suppress the formation of galaxy-sized structures, which means that it can be excluded on observational grounds [14].

It might thus be possible to determine whether dark matter is warm or cold by studying the dark matter distribution in the universe and comparing it to the CDM prediction; suppression of small-scale structure could then indicate WDM. A possible way of doing this would be to study the distribution of neutral hydrogen, which generally follows the dark matter distribution, through the Ly-α forest.
The Ly-α forest consists of a series of absorption features in the spectra of distant quasars, due to Ly-α absorption by the neutral hydrogen of the intergalactic medium (IGM) [15]. The redshift of these features depends on the distance to the absorber and the line widths depend on the size of the intervening gas structures, making it possible to reconstruct the mass distribution along the line of sight (see e.g. [16], [17] or [18]).
A complication to this scheme is that pressure in baryonic matter can mimic the free streaming of WDM [19]: small-scale perturbations in the baryonic density are generally stable against collapse due to their internal pressure and thus cannot grow, making them relatively suppressed. Additionally, thermal broadening of the lines of the observed Ly-α spectrum [20] might be wrongly interpreted as the suppression of small-scale features of the spectrum. Finally, peculiar velocities deform the matter distribution inferred from redshifts relative to the true distribution.
A way to circumvent the problems posed by the pressure and thermal effects is to realise that whereas the effect of free streaming is essentially imprinted on the initial conditions of the density field, thermal effects depend strongly on the thermal history of the IGM and thus have a different redshift dependence [21]. It might thus not be the existence of small-scale suppression in the Ly-α forest but its redshift dependence that constrains the properties of WDM.

[1] Only in extreme cases, such as for black holes, is this possible. The LSS does not consist of such strong gravitational fields.

Version of July 8, 2022– Created July 8, 2022 - 21:51

For this scheme to work, an understanding of the redshift dependence of as many influences on the Ly-α forest as possible is required. This thesis will focus on the distortions introduced by peculiar velocities in the IGM, by extracting the Ly-α forest from simulations, varying whether or not we account for peculiar velocities, and then quantifying the influence of these peculiar velocities.
Chapter 2 introduces the necessary cosmological background, namely the description and evolution of the large scale structure. Then, chapter 3 describes the Ly-α forest in more detail and proposes a characteristic spatial scale on which peculiar velocities influence the Ly-α forest. Chapter 4 briefly introduces the `SWIFT` code, a fast hydrodynamical simulation code used to produce the high-resolution simulations we use in this thesis, before describing the tools used for our analysis. Using these tools, chapter 5 presents our results. A discussion and summary of our findings is provided in chapter 6.

Chapter 2

The large scale structure of the universe

In this chapter, the relevant theoretical background will be introduced, starting with some general cosmological considerations. A formalism for describing the large scale structure (LSS) of the universe will then be introduced, after which the evolution of the LSS can be described in a Newtonian framework. Corrections and extensions due to relativistic effects will be briefly stated at the end. Far more extensive treatments of the topics presented here can be found in for example [13], [22] or [23]; see for example [24] or [25] for more cosmological background.

2.1 Cosmological background

Modern cosmology typically starts from the assumption that the universe is homogeneous and isotropic on large scales (see for example [25] and [24]). This also holds for any curvature of the universe, limiting the possible geometries to just the Friedmann-Lemaître-Robertson-Walker (FLRW) metric [24]:

$$ds^2 = c^2dt^2 - a^2(t)\left(\frac{dr^2}{1-\kappa r^2} + r^2d\theta^2 + r^2\sin^2\theta d\phi^2\right) . \tag{2.1}$$

Here, $\kappa \in \{+1, 0, -1\}$ describes the curvature of the universe, allowing for uniform negatively curved, flat or positively curved geometries. Current observations are consistent with $\kappa = 0$ [26]. The coordinates (r, θ, ϕ) are called comoving coordinates; it is to observers with constant comoving coordinates, called fundamental observers, that the universe appears homogeneous and isotropic. The physical distance between fundamental observers scales with $a(t)$, the scale factor, and hence comoving coordinates scaled with $a(t)$ are known as proper coordinates. Hereafter, spatial vectors will be written as $\mathbf{x}$ in comoving coordinates and as $\mathbf{r} = a(t)\mathbf{x}$ in proper coordinates.
An immediate consequence of this description is Hubble's law, which relates $\frac{\partial \mathbf{r}}{\partial t} = \dot{\mathbf{r}}$ to $\mathbf{r}$ itself for two fundamental observers:

$$\dot{\mathbf{r}}(t) = \dot{a}(t)\mathbf{x} = H(t)\mathbf{r}(t) , \tag{2.2}$$

Where the Hubble parameter $H(t)$ is defined as

$$H(t) \equiv \frac{\dot{a}(t)}{a(t)} . \tag{2.3}$$

Version of July 8, 2022– Created July 8, 2022 - 21:51

The present-day value of $H(t)$ is denoted H_0, but since it is relatively uncertain, results derived from it are often parametrised in terms of $h = \frac{H_0}{100\,\mathrm{km\ s^{-1}\ Mpc^{-1}}}$. Current measurements indicate $h \sim 0.7$ [11, 27], corresponding to an expanding universe.
This expansion stretches the wavelength of light as it travels cosmological distances, an effect known as the cosmological redshift. The redshift z is defined as

$$1 + z \equiv \frac{\lambda_{\mathrm{obs}}}{\lambda_{\mathrm{em}}}\,, \tag{2.4}$$

With λ_{em} the wavelength at emission and λ_{obs} at observation. If the expansion of the universe is the only cause of the redshift, the wavelength will grow proportionally to the scale factor, and we can relate the redshift to the scale factor:

$$1 + z = \frac{\lambda_{\mathrm{obs}}}{\lambda_{\mathrm{em}}} = \frac{a(t_0)}{a(t)}\,, \tag{2.5}$$

Assuming that the light was emitted at time t and is observed at time t_0, usually taken to be the present. If the expansion of the universe is monotonic (i.e. $\dot{a}$ never changes sign), the scale factor and, by the above expression, the redshift can both be used as proxy for time by fixing t_0.
To do this, the evolution of the scale factor must be found, which can be done by relating (2.1) to the contents of the universe through the field equation of general relativity. Under the restriction of homogeneity and isotropy, the energy contents of the universe can be modelled as a perfect fluid (a medium with homogeneous density ρ and uniform, isotropic pressure p), allowing one to derive the Friedmann equations from the temporal and spatial parts of the field equation [24, 28]:

$$\left(\frac{\dot{a}}{a}\right)^2 = \frac{8\pi G}{3}\rho - \frac{\kappa c^2}{a^2} + \frac{\Lambda c^2}{3}\,, \tag{2.6}$$

$$\frac{\ddot{a}}{a} = -\frac{4\pi G}{3}\left(\rho + \frac{3p}{c^2}\right) + \frac{\Lambda c^2}{3}\,. \tag{2.7}$$

Here, ρc^2 is the energy per unit proper volume, p is the pressure and Λ is the cosmological constant. According to (2.7), a positive Λ can lead to an accelerated expansion, and current observations are consistent with $\Lambda > 0$ [11, 29]. Finally, since (2.6) and (2.7) do not depend on the absolute value of a for a flat universe, we usually set $a(t_0) = 1$.
Besides Λ, two other contributions to the energy contents of the universe can be distinguished:

- Matter: a non-relativistic component, with an energy density dominated by the rest energy density; examples are baryons, cold dark matter (CDM) and warm dark matter (WDM) that has become non-relativistic. The energy density depends on the rest energy and number density of the constituent particles; the former is constant while the latter is inversely proportional to the volume, and hence $\rho_m \propto a^{-3}$.
- Radiation: a relativistic component, with an energy density dominated by the momentum of the constituent particles; examples are photons and relativistic neutrinos. Their energy density depends on both the number density of constituent particles and their momentum. This momentum depends inversely on the wavelength, which as time progresses is stretched by a factor a, so the energy density of radiation evolves as $\rho_r c^2 \propto a^{-4}$.

Customarily, densities are not quoted directly but in terms of the density parameter Ω, the ratio between the current energy density and the critical energy density

$$\rho_{\text{crit}}c^2 = \frac{3H_0^2}{8\pi G}c^2 \,. \tag{2.8}$$

This is the total density (including the contribution from Λ) such that $\kappa = 0$ in (2.6). Observations indicate that [11]

$$\Omega_\Lambda = 0.6889 \pm 0.0056 \,;$$
$$\Omega_m = 0.3111 \pm 0.0056 \,.$$

Radiation exists mostly in the form of the cosmic microwave background (CMB), which is nearly uniform blackbody radiation with a temperature of 2.72548 ± 0.00057 K [30], and relativistic neutrinos; it contributes negligibly to the present total energy density. The energy density of the universe is therefore currently dominated by the cosmological constant. However, while Λ is constant, ρ_m was larger in the past; equality occurred when

$$1 + z = \left(\frac{\Omega_\Lambda}{\Omega_m}\right)^{1/3} \equiv 1 + z_{\Lambda m} \,. \tag{2.9}$$

Thus, light with cosmological redshift greater than $z_{\Lambda m}$ was emitted when the energy density in matter was greater than that in Λ. Using the values from [11], this equality occurred around $z_{\Lambda m} = 0.3034 \pm 0.0086$. Analogously, the energy density of radiation decays faster than that of matter, and so the early universe was dominated by radiation; the redshift of matter-radiation equality is $z_{mr} \sim 3.2 \times 10^3$ [22]. Between z_{mr} and $z_{\Lambda m}$, the energy density of the universe was approximately dominated by matter.
The history of the universe might thus be divided into epochs in which a single component dominates its evolution, which significantly simplifies attempts to solve (2.6) for $a(t)$. A very relevant model is a flat matter-dominated universe; as we saw earlier, this is a reasonable approximation for the actual universe over a wide range of redshifts. In such a universe, we have $\kappa = 0$, $\rho \propto a^{-3}$ and $\Lambda \approx 0$ and (2.6) yields

$$a(t) = \left(\frac{t}{t_0}\right)^{2/3} \,, \tag{2.10}$$

Assuming $a(t_0) = 1$ and realising that $H_0 > 0$ implies $\dot{a} > 0$. From (2.10) it can be seen that

$$H = \frac{2}{3t} = \frac{H_0}{a^{3/2}} = H_0(1+z)^{3/2} \,. \tag{2.11}$$

By similarly solving (2.6) in a radiation-dominated universe, it may be found that

$$a(t) = \left(\frac{t}{t_0}\right)^{1/2} \,; \tag{2.12}$$

$$H(t) = \frac{1}{2t} \,. \tag{2.13}$$

Version of July 8, 2022– Created July 8, 2022 - 21:51

2.2 Describing the large scale structure

In reality, the universe is not perfectly homogeneous and isotropic. Galaxy surveys like the Sloan Digital Sky Survey [31] and the 2dF Galaxy Redshift Survey [32, 33] reveal that galaxies are not uniformly distributed through space, instead forming a structure known as the 'cosmic web' [34], although the universe becomes increasingly homogeneous on extremely large scales. In order to understand the implications of this large-scale structure (LSS), it is first necessary to be able to describe it.
The simplest way to describe the density field in the universe is to specify it at every point at any given time by giving $\rho(\mathbf{r}, t)$. However, since the evolution of the background density is well-understood through (2.6) and (2.7) it is often more useful to think of inhomogeneities as perturbations to the background density. In that case, the density field can be described with the density contrast $\delta(\mathbf{r}, t)$, the relative deviation from the average density at a given point and time:

$$\rho(\mathbf{r}, t) = \rho_0(t)\left(1 + \delta(\mathbf{r}, t)\right) , \tag{2.14}$$

With $\rho_0(t)$ the average density. By this definition, $\langle\delta\rangle = 0$, where $\langle\cdot\rangle$ denotes a volume average over a sufficiently large volume.
Current theories place the origin of the LSS in quantum fluctuations in the very early universe, which were then stretched to macroscopic scales by inflation [22]. Hence, the perturbations would be expected to be initiated randomly, so that much of the relevant physics is encoded not in the density field itself, but in its statistical properties. One of the ways these can be described is through the two-point correlation function ξ of the density contrast, which measures the degree to which the density contrast at different points correlates and is defined as

$$\xi\left(R\right) = \left\langle \delta\left(\mathbf{r}, t\right) \delta\left(\mathbf{r} + \mathbf{R}, t\right)\right\rangle . \tag{2.15}$$

The angular brackets in principle denote an ensemble average, i.e. an average over the outcomes of all possible realisations of the random process that created the initial perturbations. Because only a single realisation is available for observation, we assume ergodicity, meaning that an ensemble average can be approximated by a volume average [13]; we will not explicitly distinguish between ensemble and volume averages. Because the universe is homogeneous and isotropic on very large scales, the statistical properties of the density field are as well, implying that ξ is independent of the choice for $\mathbf{r}$ and the direction of $\mathbf{R}$. ξ can be related to the variance σ^2 in δ:

$$\begin{aligned}\sigma^2(t) &= \langle\delta^2(\mathbf{r}, t)\rangle - \langle\delta(\mathbf{r}, t)\rangle^2 \\ &= \xi(0) .\end{aligned} \tag{2.16}$$

Additionally we may consider the density field not in real space but in Fourier space. If the universe is flat, plane waves form a complete basis and any field can be written as a superposition of them. Therefore, define the fourier transform and its inverse as

$$\delta_{\mathbf{k}}(t) = \int_V \delta(\mathbf{r}, t) e^{-i\mathbf{k}\cdot\mathbf{r}} d^3\mathbf{r} ; \tag{2.17}$$

$$\delta(\mathbf{r}, t) = \int_{\mathbb{R}^3} \delta_{\mathbf{k}}(t) e^{i\mathbf{k}\cdot\mathbf{r}} \frac{d^3\mathbf{k}}{(2\pi)^3} , \tag{2.18}$$

Version of July 8, 2022– Created July 8, 2022 - 21:51

With V a volume over which the universe is assumed to be periodic and $\mathbf{k}$ the (proper) wave vector; $\langle\delta\rangle = 0$ implies that $\langle\delta_{\mathbf{k}}\rangle = 0$ as well. ξ can now be written in terms of the fourier components $\delta_{\mathbf{k}}$ (suppressing the time dependence for the sake of clarity):

$$\begin{aligned}\xi(R) &= \langle\delta(\mathbf{r})\delta(\mathbf{r}+\mathbf{R})\rangle \\ &= \frac{1}{V}\int_V\int_{\mathbb{R}^3}\int_{\mathbb{R}^3}\delta_{\mathbf{k}}\delta_{\mathbf{k}'}e^{i\mathbf{k}\cdot\mathbf{r}}e^{i\mathbf{k}'\cdot(\mathbf{r}+\mathbf{R})}\frac{d^3\mathbf{k}}{(2\pi)^3}\frac{d^3\mathbf{k}'}{(2\pi)^3}d^3\mathbf{r} \\ &= \int_{\mathbb{R}^3}\frac{1}{V}\left|\delta_{\mathbf{k}}\right|^2 e^{-i\mathbf{k}\cdot\mathbf{R}}\frac{d^3\mathbf{k}}{(2\pi)^3}\,. \end{aligned} \tag{2.19}$$

Here, the following identities have been used:

$$\frac{1}{(2\pi)^3}\int_V e^{i(\mathbf{k}+\mathbf{k}')\cdot\mathbf{r}}d^3\mathbf{r} = \delta^D\left(\mathbf{k}+\mathbf{k}'\right)\;; \tag{2.20}$$

$$\delta_{-\mathbf{k}} = \delta^*_{\mathbf{k}}\,, \tag{2.21}$$

With δ^D the Dirac delta distribution; both of these can be proven using the definition of the Fourier transform. $\delta_{\mathbf{k}}$ can in principle vary between different realisations of the universe, but ξ should not, so it is necessary to introduce another (ensemble) average:

$$\xi(R) = \int_{\mathbb{R}^3}\frac{1}{V}\langle\left|\delta_{\mathbf{k}}\right|^2\rangle e^{-i\mathbf{k}\cdot\mathbf{R}}\frac{d^3\mathbf{k}}{(2\pi)^3}\,. \tag{2.22}$$

It is clear that ξ is the fourier transform of a quantity known as the power spectrum P:

$$P(k) = P(|\mathbf{k}|) = \frac{1}{V}\langle\left|\delta_{\mathbf{k}}\right|^2\rangle\,, \tag{2.23}$$

Where the first equality holds due to the isotropy of the universe. Finally, note that

$$\begin{aligned}\sigma^2(t) &= \xi(0) \\ &= \int_{\mathbb{R}^3}P(k)\frac{d^3\mathbf{k}}{(2\pi)^3} \\ &= \int_0^\infty\frac{k^3}{2\pi^2}P(k)\frac{dk}{k} \equiv \int_0^\infty\Delta^2(k)\frac{dk}{k}\,, \end{aligned} \tag{2.24}$$

So the dimensionless power spectrum $\Delta^2(k) = \frac{k^3P(k)}{2\pi^2}$ describes the contribution of fourier modes in a logarithmic bin of k to the variance in δ.
In the next section it will be shown that the evolution of δ can initially be described using a linear differential equation. The principle of superposition then implies that all fourier components $\delta_{\mathbf{k}}$ evolve independently and according to the same law, and hence we can separate the time evolution of the power spectrum from its k-dependence. Furthermore, it might be possible to predict the power spectrum $P_i(k)$ as produced by the initial mechanism which introduced inhomogeneities in the density field. This allows us to write the power spectrum as

$$P(k,t) = P_i(k)T^2(k)D^2(t)\,. \tag{2.25}$$

Here, $D(t)$ is the growth factor describing by how much a perturbation has grown at time t relative to some initial time t_i after which the time-evolution can be separated from its k-dependence; due to relativistic effects, t_i must be the moment (in the matter epoch) at which the largest mode of interest has a wavelength on the scale on which Newtonian gravity is a good approximation to general relativity [22]. The transfer function $T(k)$ describes the evolution between the moment $P_i(k)$ was set and t_i.

2.3 The evolution of the large scale structure

The LSS that can be described by the formalism in section 2.2 is not static but evolves as gravity attempts to concentrate matter in high-density regions. If we consider scales much bigger than the mean free path of particles in the universe, the contents of the universe can be modelled as a self-gravitating fluid. On scales much smaller than the horizon distance[1], causality is essentially instantaneous and so in a matter-dominated universe[2], general relativity reduces to Newtonian gravity on such small scales. The condition of matter dominance is satisfied for a large range of redshifts, making the Newtonian treatment relevant for most observationally interesting redshifts.
The Newtonian system of equations describing a self-gravitating fluid consists of the continuity equation, describing conservation of mass, the Euler equation, describing the force on a fluid element, and the Poisson equation, describing gravity:

$$\frac{\partial \rho}{\partial t} + \nabla \cdot (\mathbf{v}\rho) = 0 \, ; \tag{2.26}$$

$$\frac{\partial \mathbf{v}}{\partial t} + (\mathbf{v} \cdot \nabla)\, \mathbf{v} = -\frac{1}{\rho}\nabla p - \nabla \Phi \, ; \tag{2.27}$$

$$\nabla^2 \Phi = 4\pi G \rho \, . \tag{2.28}$$

All spatial derivatives are with respect to proper coordinates and the partial time derivative is evaluated at a fixed proper position; $\mathbf{v}$ is the (proper) velocity field of the fluid and Φ is the gravitational potential. Finally, this system must be closed by an equation of state $p = p(\rho)$ relating the pressure p to the density ρ.
Since gravity is an attractive force, it will tend to enhance contrasts in the density field. Any inhomogeneities in the present-day density field are thus expected to have grown from small primordial perturbations, suggesting that the initial stages of structure formation may be described using linear perturbation theory applied to (2.26)-(2.28). All quantities should then be written as their value in a completely homogeneous and isotropic universe, denoted by a subscript 0, and a small perturbation:

$$\begin{aligned} \rho(\mathbf{r}, t) &= \rho_0(t)\,(1 + \delta(\mathbf{r}, t)) \, ; \\ \mathbf{v}(\mathbf{r}, t) &= \mathbf{v}_0(\mathbf{r}, t) + \mathbf{u}(\mathbf{r}, t) \, ; \\ \Phi(\mathbf{r}, t) &= \Phi_0(\mathbf{r}, t) + \Psi(\mathbf{r}, t) \, . \end{aligned}$$

The equation of state $p = p(\rho)$ may be expanded around ρ_0 to find $p_0 = p(\rho_0)$ and

$$\delta p(\mathbf{r}, t) = \frac{\partial p}{\partial \rho}\rho_0 \delta(\mathbf{r}, t) = v_s^2 \rho_0 \delta(\mathbf{r}, t) \, , \tag{2.29}$$

Where $v_s^2 = \frac{\partial p}{\partial \rho}$ is the speed of sound squared. $\mathbf{v}_0$ can be identified with the Hubble flow $H(t)\mathbf{r}$, since both are present even in a completely homogeneous and isotropic universe. $\mathbf{u}$ can then be expressed in terms of the comoving coordinates and $a(t)$:

$$\begin{aligned} \mathbf{v} &= \dot{\mathbf{r}} \\ \mathbf{v}_0 + \mathbf{u} &= H(t)\mathbf{r} + a\dot{\mathbf{x}} \\ \mathbf{u} &= a\dot{\mathbf{x}} \, . \end{aligned} \tag{2.30}$$

[1] The horizon distance, which may be approximated as the Hubble length $L_H = c/H$, is the size of the causally connected universe.

[2] Matter dominance is required because Newtonian gravity neglects the gravitational influence of pressure, which is significant for radiation and dark energy.

Version of July 8, 2022– Created July 8, 2022 - 21:51

The general scheme is now to insert the perturbed quantities into (2.26)-(2.28) and keep only terms up to linear order in the perturbations. For example, (2.26) becomes

$$\left(\frac{\partial \rho_0}{\partial t} + \nabla \cdot (\mathbf{v}_0 \rho_0)\right)(1+\delta) + \rho_0 \frac{\partial \delta}{\partial t} + \rho_0 \mathbf{v}_0 \cdot \nabla \delta + \nabla \cdot \rho_0 \mathbf{u} = 0 \,. \tag{2.31}$$

For vanishing perturbations, only the first term in brackets remains. However, the perturbations do not change the background quantities, so these first terms must always vanish. Since ρ_0 is homogeneous, it has vanishing spatial derivatives:

$$\begin{aligned} \rho_0 \frac{\partial \delta}{\partial t} + \rho_0 \mathbf{v}_0 \cdot \nabla \delta + \rho_0 \nabla \cdot \mathbf{u} &= 0 \\ \frac{d\delta}{dt} &= -\nabla \cdot \mathbf{u} \,, \end{aligned} \tag{2.32}$$

Where $\frac{d}{dt} \equiv \frac{\partial}{\partial t} + \mathbf{v}_0 \cdot \nabla$ is the total (or Lagrangian) time derivative for a fundamental observer. The Euler and Poisson equations (2.27) and (2.28) can be treated similarly: write all quantities as a background and a perturbation, cancel the pure background terms since they must equal for vanishing perturbations and discard terms that are of higher than linear order in the perturbations. Furthermore, note that if $\mathbf{v}_0 = H(t)\mathbf{r}$ it can be straightforwardly shown that

$$(\mathbf{u} \cdot \nabla)\, \mathbf{v}_0 = H(t)\mathbf{u} \,. \tag{2.33}$$

(2.27) and (2.28) now linearise to

$$\frac{d\mathbf{u}}{dt} + H(t)\mathbf{u} = -v_s^2 \nabla \delta - \nabla \Psi \,; \tag{2.34}$$

$$\nabla^2 \Psi = 4\pi G \rho_0 \delta \,. \tag{2.35}$$

In principle, (2.32), (2.35) and (2.34) form a complete description of the linear stages of structure formation. However, they are more conveniently written in comoving instead of proper coordinates. In comoving coordinates, an observer moving with the Hubble flow $\mathbf{v}_0$ is stationary, and hence $\frac{d}{dt} \to \frac{\partial}{\partial t}$, a partial time derivative evaluated at constant comoving coordinates. Also, note that

$$\nabla = \frac{\partial}{\partial \mathbf{r}} = \frac{1}{a(t)} \frac{\partial}{\partial \mathbf{x}} \,. \tag{2.36}$$

Redefining $\nabla = \frac{\partial}{\partial \mathbf{x}}$ thus means that $\nabla \to \frac{1}{a}\nabla$. Furthermore, recall that $\mathbf{u} = a\dot{\mathbf{x}}$ so

$$\dot{\mathbf{u}} = \dot{a}\dot{\mathbf{x}} + a\ddot{\mathbf{x}} = H(t) a \dot{\mathbf{x}} + a\ddot{\mathbf{x}} \,. \tag{2.37}$$

The system of linear equations describing the linear stage of structure formation in comoving coordinates thus becomes

$$\dot{\delta} = -\nabla \cdot \dot{\mathbf{x}} \,; \tag{2.38}$$

$$\ddot{\mathbf{x}} + 2H(t)\dot{\mathbf{x}} = -\frac{v_s^2}{a^2} \nabla \delta - \frac{1}{a^2} \nabla \Psi \,; \tag{2.39}$$

$$\nabla^2 \Psi = 4\pi G a^2 \rho_0 \delta \,, \tag{2.40}$$

With the dot now denoting a partial time derivative at fixed comoving coordinates. Combining the time derivative of (2.38) with (2.40) and the divergence of (2.39), we obtain the central equation in the description of the Newtonian evolution of the LSS:

$$\ddot{\delta} + 2H(t)\dot{\delta} - \frac{v_s^2}{a^2} \nabla^2 \delta = 4\pi G \rho_0 \delta \,. \tag{2.41}$$

2.3.1 The influence of pressure: the Jeans and filtering scales

Equation (2.41) can be solved for various cosmological models. A first and unrealistic example would be the case of a static universe, with $H(t) = 0$ and $a(t)$ constant. We can take the Fourier transform of (2.41) by noting that for the comoving gradient of a function f, we have

$$[\nabla f]_{\mathbf{k}} = \left[\frac{\partial}{\partial \mathbf{x}} \int_{\mathbb{R}^3} f_{\mathbf{k}} e^{i\mathbf{k}\cdot a\mathbf{x}} \frac{d^3\mathbf{k}}{(2\pi)^3}\right]_{\mathbf{k}} = ia\mathbf{k} f_{\mathbf{k}} \,. \tag{2.42}$$

Thus, taking the fourier transform of (2.41) and making the ansatz $\delta_{\mathbf{k}} \propto e^{i\omega t}$ yields

$$-\omega^2 + v_s^2 k^2 = 4\pi G\rho_0 \,. \tag{2.43}$$

The ansatz now corresponds to a perturbation oscillating with constant amplitude if $\omega \in \mathbb{R}$; such perturbations are stable against collapse. However, if ω is complex, the amplitude of δ changes exponentially with time; if a growing mode is present, the perturbation will collapse and form a non-linear structure which is no longer adequately described by linear perturbation theory. The boundary between these two cases can be drawn at $\omega^2 = 0$, such that

$$\begin{aligned} v_s^2 k_J^2 &= 4\pi G\rho_0 \\ \lambda_J = \frac{2\pi}{k_J} &= \sqrt{\frac{\pi v_s^2}{G\rho_0}} \,. \end{aligned} \tag{2.44}$$

λ_J is known as the Jeans scale. Perturbations with smaller wavelengths ($k > k_J$) are supported against gravitational collapse by pressure, while perturbations on larger scales ($k < k_J$) can overcome their internal pressure and collapse.
In reality, the universe expands, which alters the evolution of a plane wave through the H-dependent term in (2.41); this alters the actual scale on which a perturbation can support itself against collapse. Furthermore, we will see that the temperature of the IGM can change significantly during the history of the universe. This is relevant because the temperature, through v_s, partially determines the value of k_J and so a significant and rapid change in temperature translates to a significant and rapid change in k_J. However, since gas can't rearrange itself arbitrarily fast, perturbations that suddenly find themselves with $k < k_J$ don't collapse immediately. Each of these reasons (the alteration of a plane wave by the expansion of the universe and the finite response time to a change in temperature) imply that a better estimate of the wavenumber above which perturbations are stable against collapse is the filtering scale k_F from [35]:

$$\frac{1}{k_F^2(a)} = 3a \int_0^a \frac{1}{a'^2 k_J^2(a')} \left(1 - \left(\frac{a'}{a}\right)^{1/2}\right) da' \,. \tag{2.45}$$

Note that to derive this expression from the one given in [35], it was assumed that $\Omega_m = 1$, which is appropriate for our current treatment.

2.3.2 The matter-dominated universe

As a more realistic model, we might consider a dark matter dominated universe. A universe completely dominated by matter has (2.10) as scale factor, (2.11) as Hubble

parameter and because the universe is spatially flat, $\rho_0(t_0) = \rho_{\text{crit}}$ from (2.8), so that

$$\rho_0(t) = \frac{\rho_0(t_0)}{a^3(t)} = \frac{1}{6\pi G t^2} \,. \tag{2.46}$$

We can model dark matter as only interacting gravitationally, so it must have zero pressure. Combining this density with (2.11) and (2.41) then yields

$$\ddot{\delta} + \frac{4}{3t}\dot{\delta} = \frac{2}{3t^2}\delta \,. \tag{2.47}$$

If we make the ansatz that $\delta \propto t^\alpha$, we find $\alpha = \frac{2}{3}$ or $\alpha = -1$; the decaying mode cannot have been important since structure has grown from small initial perturbations. Therefore, in a dark matter dominated universe perturbations evolve as

$$\delta(\mathbf{r}, a) \propto a \,. \tag{2.48}$$

In this particular model, the growth factor from (2.25) therefore is $D(t) = a(t)/a(t_i)$. In an even more realistic model, baryons are also accounted for. Baryons only interact with dark matter gravitationally and hence in (2.26)-(2.28) only (2.28) is not applicable to each component (baryons or dark matter) individually. Therefore (2.41) holds for every component individually as long as we replace the right hand side by a sum over the components, and the correct form of (2.41) for baryons in a universe containing both dark matter (subscript *dm*) and baryons (subscript *b*) is a system of equations:

$$\ddot{\delta}_{dm} + 2H(t)\dot{\delta}_{dm} = 4\pi G\rho_0 \left(f_b\delta_b + f_{dm}\delta_{dm}\right) \,; \tag{2.49}$$

$$\ddot{\delta}_b + 2H(t)\dot{\delta}_b - \frac{v_s^2}{a^2}\nabla^2\delta_b = 4\pi G\rho_0 \left(f_b\delta_b + f_{dm}\delta_{dm}\right) \,, \tag{2.50}$$

With f_i the fractional contribution of the respective components to the total average density (so $f_b + f_{dm} = 1$). In the limit $f_b \to 0$, (2.49) reduces to (2.47) with solution (2.48). On the other hand, taking the Fourier transform of (2.50) in this limit yields

$$\ddot{\delta}_{b,\mathbf{k}} + 2H(t)\dot{\delta}_{b,\mathbf{k}} = 4\pi G\rho_0 f_{dm}\delta_{dm,\mathbf{k}} - v_s^2 k^2 \delta_{b,\mathbf{k}} \,. \tag{2.51}$$

For large scales, $k \to 0$ and the right hand side of this equation becomes identical to that of (2.49) in the limit $f_b \to 0$, while the form of the left hand side is identical to that of (2.49). Therefore, on large scales, baryons follow the dark matter distribution, while their distributions differ on small scales where pressure is relevant. [35] shows that the effect of this pressure can be accurately described as

$$\frac{\delta_{b,\mathbf{k}}}{\delta_{dm,\mathbf{k}}} \propto e^{-\frac{k^2}{k_F^2}} \,. \tag{2.52}$$

The effect of the pressure is thus to suppress $\delta_{b,\mathbf{k}}$ for $k > k_F$, which is sensible in the light of the discussion from section 2.3.1. This cutoff persists into the power spectrum, which depends on the squared amplitude of the Fourier components:

$$\frac{P_b(k,t)}{P_{dm}(k,t)} = \frac{\Delta_b^2(k,t)}{\Delta_{dm}^2(k,t)} \propto e^{-\frac{2k^2}{k_F^2}} \,. \tag{2.53}$$

Since k_F takes on a finite value for all realistic thermal histories, we expect the power spectrum to always contain this so-called pressure cutoff.

In fact, (2.48) produces an apparent contradiction between observations. At last scattering of the CMB at $z_{\text{rec}} \sim 1000$, radiation is still tightly coupled to the baryons, and hence CMB temperature anisotropies of $\delta T/T \sim 10^{-5}$ [11] imply similar baryonic density contrasts $\delta_b \sim 10^{-5}$. If these perturbations then grew as implied by (2.48)[3] their amplitude would have grown by a factor $a^{-1}(t_{\text{rec}}) = 1 + z_{\text{rec}} \sim 1000$, resulting in perturbations with $\delta_b \sim 10^{-2}$. This is still well within the linear regime, and thus directly contradicts the abundance of highly nonlinear structures we can observe today. The solution to this contradiction lies in the fact that dark matter does not interact electromagnetically, and hence it already forms structures before the onset of the matter epoch [22]. Once the baryons decouple from the CMB, they can simply move into the dark matter potential wells, temporarily evolving much faster than (2.48) implies.

2.3.3 Peculiar velocities

Considering (2.38), peculiar velocities play a central role in the formation of structure as they carry the matter that accretes into structures. Since only this concentrating function is relevant for structure formation, a solenoidal velocity field with $\nabla \cdot \mathbf{u} = 0$ does not cause perturbations to the density, pressure or potential and so these kinds of fields are usually neglected[4]. $\mathbf{u}$ is thus assumed to be, at least initially, a conservative field. If the matter has negligible initial peculiar velocities, $\mathbf{u}$ must be gravitationally induced and hence a function of the gravitational acceleration:

$$\mathbf{u} = F(t)\mathbf{g} = -F(t)\frac{\partial \Psi}{\partial \mathbf{r}} = -\frac{F(t)}{a(t)}\nabla\Psi = a\dot{\mathbf{x}} \,, \tag{2.54}$$

For some universal function $F(t)$. Combining this with (2.38) and (2.40) yields

$$F(t) = \frac{\dot{\delta}}{4\pi G\rho_0 \delta} \,. \tag{2.55}$$

Since we assume the linear regime, we may also relate $\mathbf{u}$ to the initial state of the universe. Recall that the growth factor $D(t)$ was defined as the factor by which any Fourier component $\delta_{\mathbf{k}}$ has grown since $t_i < t$, so that

$$\delta(\mathbf{x}, t) = D(t)\delta(\mathbf{x}, t_i) \,, \tag{2.56}$$

With the potential perturbation as a function of comoving position to remove ambiguity with regard to the time derivative. By considering how the right hand side of (2.40) relates to the conditions at time t_i, it may be shown that

$$\Psi(\mathbf{x}, t) = \frac{a(t_i)}{a(t)} D(t)\Psi(\mathbf{x}, t_i) \,. \tag{2.57}$$

By combining this with (2.55) and (2.56) we can obtain the peculiar velocities as

$$\mathbf{u} = -\frac{\dot{D}(t)}{4\pi G\rho_0(t_i)}\frac{a(t)}{a^2(t_i)}\nabla\Psi(\mathbf{x}, t_i) = -\frac{2\dot{a}(t)a(t)}{3H_0^2}\nabla\Psi(\mathbf{x}, t_i) \,, \tag{2.58}$$

[3] In reality, baryons remain strongly coupled to the CMB until $z \sim 100$ [23], which suppresses the growth of baryonic perturbations.

[4] Furthermore, since they represent rotations in the cosmic medium, we can consider a volume element of mass m performing such a rotation with characteristic radius l and rotation speed u^T. Its angular momentum is then $L \sim mlu^T$, and since L and m are conserved and $l \propto a(t)$, u^T must decay [22], further cementing its irrelevance.

Version of July 8, 2022– Created July 8, 2022 - 21:51

Where the last equality used the fact that we assumed a flat matter-dominated universe, so that $\rho_0(t) = \rho_{\text{crit}} a^{-3}(t)$ and $D(t) = a(t)/a(t_i)$. (2.58) implies that $\mathbf{u}$ grows with time and is directed towards maxima in the density.

2.3.4 Warm dark matter free streaming

A final effect we can describe is free streaming by WDM. This effect occurs because WDM, while relativistic, cannot be gravitationally bound. If the primordial velocities of WDM are isotropically distributed there will be more particles moving out of a density concentration than moving into it; such a concentration will thus smooth out over time. Free streaming doesn't significantly affect large-scale structures because WDM cannot move substantially out of such a structure during its (relatively brief) relativistic stage, but small-scale structures may be significantly suppressed. Free streaming thus introduces another cutoff to the power spectrum, with a cutoff scale known as the free streaming length λ_{fs}. A rigorous treatment such as presented in [22] yields a cutoff scale similar to (2.44), with v_s^2 replaced by $\langle \frac{1}{u^2} \rangle^{-1}$, a typical[5] intrinsic (i.e. not gravitationally-induced) speed squared. A more intuitive scale is the free streaming horizon λ_{fsh}, the maximum proper distance a WDM particle will typically travel [12]. If a WDM particle has proper speed $v(t) = a(t)\frac{dx}{dt}$, then

$$\lambda_{\text{fsh}}(t) = a(t) \int_0^{\lambda_{\text{fsh}}/a(t)} dx = a(t) \int_0^t \frac{v(t')}{a(t')} dt' \, . \tag{2.59}$$

If the WDM is completely relativistic until some time t_{nr} in the radiation epoch and then becomes essentially stationary, (2.59) may be evaluated using (2.12), yielding

$$\lambda_{\text{fsh}}(t) = \frac{2}{3} a(t_{\text{nr}}) c t_{\text{nr}} a(t) \, . \tag{2.60}$$

This is of course a strongly simplified picture, but it is a general principle that λ_{fsh} is set during the radiation epoch (WDM becomes non-relativistic during this epoch) and then barely evolves save scaling with $a(t)$ [12]. Any difference between WDM and CDM is thus not primarily in their initial power spectrum or evolution in the matter epoch, but in their transfer function in the form of a suppression of small scale structures.

[5] To be precise: averaged with the phase space density as weight.

Chapter 3

The Ly-α forest

As was indicated in section 2.3.4, it is in principle possible to discriminate between cold and warm dark matter (CDM and WDM) through the power spectrum of the LSS because WDM suppresses structures on scales smaller than λ_{fsh} by free streaming. Therefore, it is of considerable interest to determine the power spectrum at these small scales. Often, galaxies are used to trace the cosmic density field, with surveys such as [31] and [32] mapping the position and redshift of many thousands of galaxies. There are however several drawbacks to galaxies as density tracers. For example, they have a galaxy-type dependent bias for denser environments [13, 14], they are highly nonlinear structures that may deviate from the linear structure, and intergalactic distances are of the order $\sim$ Mpc, while λ_{fs} may be as small as $\sim 0.1h^{-1}$ Mpc at $z = 0$ [7]. A more promising approach to reconstruct the small scale power spectrum is through the Ly-α forest: a series of absorption features in quasar spectra due to Ly-α absorption by neutral hydrogen in the intergalactic medium (IGM) [15]. Since the redshift of these absorption features depends on the distance to the absorbing structures (considering (2.4) and the fact that $t_0 - t$ is set by the distance due to the finite speed of light), the Ly-α forest might share statistical properties with the cosmic density field.
In this chapter, the IGM, the source of the Ly-α forest, will be introduced first. Subsequently, an expression for the absorption spectrum produced by the IGM will be derived, after which section 3.3 will give a brief description of the relation between the Ly-α forest and the power spectrum $P(k)$ of dark matter. Finally, a phenomenological expression for the scale on which peculiar velocities impact the FPS will be proposed. Much of the material presented here is based on [36] and [23].

3.1 The ionisation state of the intergalactic medium

The IGM consists of all gas between galaxies, which is mostly hydrogen and helium, although it has a detectable metallicity [37, 38]. Following recombination, this gas was mostly neutral; it was this fact that allowed the cosmic microwave background to propagate freely. As structures grew, they eventually collapsed into nonlinear structures such as Population III-stars, galaxies and quasars, and due to the ionising radiation these objects produce, the IGM was re-ionised [23]. This also significantly raised the temperature of the IGM [39]. Since the Ly-α transition has a relatively large cross

section, a very low density of neutral hydrogen suffices for complete absorption of the Ly-α line. As a result, a neutral hydrogen fraction of just 10^{-6} may already be enough to create a spectral region of complete absorption in the spectrum of a quasar, known as a Gunn-Peterson trough [40]. The fact that such a trough only arises in spectra of quasars with $z \gtrsim 6$ [41] indicates that re-ionisation was almost complete, and that the current IGM consists mainly of ionised hydrogen.

To describe the ionisation state of the IGM, we typically assume dynamical ionisation equilibrium, in which the rates of ionisation and recombination are equal. The rate $\mathcal{R}_{ab}$ of a reaction between any two particle species a and b can be written as

$$\mathcal{R}_{ab} = \langle v_{\text{rel}} \sigma_{ab} \rangle n_a n_b \, . \tag{3.1}$$

Here, v_{rel} is the relative speed between particles of species a and b, σ_{ab} is the cross section of the reaction (which may depend on v_{rel}), and n_a and n_b are the respective number densities.

There are two main venues of ionisation: collisional ionisation and photo-ionisation. Since the rate of the former rapidly decreases for temperatures below $T \sim 13.6\,\text{eV}/k_B \sim 10^5$ K, we focus on the latter. For a given radiation field, the energy density $u(\nu)$ in a frequency range $[\nu, \nu + d\nu]$ is [42]

$$u(\nu) = \frac{4\pi J(\nu)}{c} \, , \tag{3.2}$$

Where $J(\nu)$ is the average intensity. The number density $n_\gamma(\nu)$ of photons within this frequency range is thus $u(\nu)$ divided by $h\nu$, the energy of a single photon, and the number density of potentially ionising photons is n_γ integrated above the ionisation threshold frequency ν_i. Since the relative speed between an photon and a hydrogen atom is always c and the ionisation cross section σ_i is frequency-dependent, (3.1) yields a rate of photo-ionisation of neutral hydrogen of

$$\mathcal{R}_{\text{photo}} = \int_{\nu_i}^{\infty} \sigma_i(\nu) c \frac{4\pi J(\nu)}{h\nu c} d\nu \; n_{\text{HI}} \equiv \Gamma_{\text{HI}} n_{\text{HI}} \, . \tag{3.3}$$

For hydrogen $h\nu_i = 13.6\,\text{eV}$, and n_{HI} is the neutral hydrogen number density. Both $\mathcal{R}_{\text{photo}}$ (with units $\text{cm}^{-3}\ \text{s}^{-1}$) and Γ_{HI} (with units s^{-1}) may be referred to as the photo-ionisation rate, so we will quote the symbol wherever necessary.

Recombination on the other hand can only happen collisionally. Thus, for number densities n_e and n_{HII} of electrons and protons respectively and an interaction cross section σ_{rec}, (3.1) yields a recombination rate of

$$\mathcal{R}_{\text{rec}} = \langle \sigma_{\text{rec}} v_{\text{rel}} \rangle n_e n_{\text{HII}} = \alpha_{\text{HII}}(T) n_e n_{\text{HII}} \, . \tag{3.4}$$

Again, both $\mathcal{R}_{\text{rec}}$ (with units $\text{cm}^{-3}\ \text{s}^{-1}$) and α_{HII} (with units $\text{cm}^3\ \text{s}^{-1}$) may be referred to as the recombination rate; α_{HII} depends on the temperature because v_{rel} is set by the thermal velocities in the gas (and σ_{rec} is set by v_{rel}). Approximately, $\alpha_{\text{HII}} \propto T^{-0.7}$ [23].

The rate of change in n_{HI} is now set by the difference between the recombination rate $\mathcal{R}_{\text{rec}}$, which produces more neutral hydrogen, and $\mathcal{R}_{\text{photo}}$, which destroys it. The assumption of ionisation equilibrium thus demands that

$$\begin{aligned} \frac{dn_{\text{HI}}}{dt} &= 0 \\ \alpha_{\text{HII}}(T) n_e n_{\text{HII}} - \Gamma_{\text{HI}} n_{\text{HI}} &= 0 \\ n_{\text{HI}} &= \frac{\alpha_{\text{HII}}(T)}{\Gamma_{\text{HI}}} n_e n_{\text{HII}} \, . \end{aligned} \tag{3.5}$$

Version of July 8, 2022– Created July 8, 2022 - 21:51

This can be further simplified by assuming that the hydrogen is almost completely ionised, hence $n_e \approx n_{\mathrm{HII}} \approx n_H$, the total hydrogen density[1]:

$$n_{\mathrm{HI}} = \frac{\alpha_{\mathrm{HII}}}{\Gamma_{\mathrm{HI}}} n_H^2 \, . \tag{3.6}$$

Γ_{HI} directly depends on the ionising radiation background and thus has to be modelled numerically (as proposed in for example [39]). α_{HII} can be expressed as a function of the IGM temperature [43]. In turn, the IGM temperature T is set by a balance between adiabatic cooling due to the expansion of the universe, changes in particle abundances and heating by radiation. Together, these processes produce a temperature-density relation [43] that can be parameterised as a power law (with δ the contrast in the baryonic density):

$$T = T_0 \, (1+\delta)^{\gamma - 1} \, . \tag{3.7}$$

T_0 and γ evolve with redshift, as the universe is initially heated to a uniform temperature during re-ionisation and then cools most rapidly in the least dense regions.

3.2 The optical depth of the Ly-α forest

In order to use the Ly-α forest as a cosmological probe, it is necessary to relate the observed spectrum to the properties of the IGM. This can be done using the equation for radiative transport:

$$\frac{dI_\nu}{dr} = j_\nu - \alpha_\nu I_\nu \, . \tag{3.8}$$

Here, I_ν is the intensity in units of power per unit area, frequency and solid angle, r is the proper distance, j_ν is the emission coefficient describing the power the medium emits per unit volume, frequency and solid angle, and α_ν is the absorption coefficient giving the fraction of absorbed intensity per unit proper length [42]. Due to the high ionisation degree and low density, emission from the IGM is usually neglected. The resulting differential equation can then be immediately solved to yield

$$I_\nu = I_\nu^0 e^{-\tau(\nu)} \, . \tag{3.9}$$

Here, I_ν^0 is the initial quasar spectrum and the optical depth $\tau(\nu)$ is the integral of α_ν over the entire line of sight. What is typically done is that I_ν is divided by a calculated quasar spectrum I_ν^0 to obtain the transmission or flux F, a process known as 'continuum fitting'. The advantage of using F is that we may now characterise the entire spectrum with a single parameter:

$$F(\nu) = e^{-\tau(\nu)} \, . \tag{3.10}$$

Hence, calculating the optical depth is the central aim of this section.
Assuming that the absorption is due to neutral hydrogen with number density n_{HI} and Ly-α absorption cross section $\sigma(\nu)$, the optical depth may be written as

$$\tau(\nu) = \int n_{\mathrm{HI}}(r) \sigma(\nu) dr \, . \tag{3.11}$$

[1] Helium may also be ionised. This slightly increases n_e, but is often ignored because of the lower number density of helium and the higher ionisation energy.

However, the frequency in the integral can, in the current context, not be the same as the one at which τ is evaluated due to the cosmological redshift: according to (2.5), light is redshifted as it travels by the expansion of the universe. Thus, light that has frequency ν on observation had a higher frequency at some distance r. To account for this, we might use the redshift as a proxy for distance in the following way:

$$\begin{aligned} dr &= cdt \\ &= \frac{c}{H(t)} \frac{1}{a} \frac{da}{dt} dt \\ &= \frac{c}{H(a)} \frac{da}{a} \\ &= \frac{cdz}{H(z)\,(1+z)}\,, \end{aligned} \tag{3.12}$$

Where the definition of H in (2.3), (2.5) with $a(t_0) = 1$ and the fact that the proper speed of light is always c were used. Thus, to every distance r we may assign a redshift z, and light that is observed at frequency ν had a frequency ν' at distance r such that

$$\nu = \frac{\nu'}{1+z}\,, \tag{3.13}$$

Where z is the redshift associated with distance r. It is at rest frame frequency ν' that the IGM at distance r, or redshift z, produces absorption that is observed at frequency ν, and hence (3.11) may be combined with (3.12) and (3.13) to yield [40]

$$\tau(\nu) = \int n_{\mathrm{HI}}(z) \sigma\left((1+z)\,\nu\right) \frac{cdz}{H(z)(1+z)}\,. \tag{3.14}$$

So far, it has been implicitly assumed that the redshift is entirely cosmological in origin. In reality, the IGM has peculiar velocities both on large scales as described in section 2.3.3 and due to thermal motion of the gas; both cause an additional Doppler shift.
We can incorporate the thermal motion by broadening the interaction cross section. The absorption cross section of a single particle may be described as

$$\sigma(\nu) = \sigma_0 \phi\left(\nu - \nu_\alpha\right)\,, \tag{3.15}$$

Where $\phi(\nu)$ is the line profile and integrates to 1 over all frequencies, σ_0 is an amplitude, and ν_α is the rest frame Ly-α frequency. Quantum mechanics then shows [42] that in CGS units

$$\sigma_0 = \frac{\pi e^2}{m_e c} f_{12}\,, \tag{3.16}$$

Where $f_{12} = 0.416$ is the oscillator strength of the Ly-α transition.
If we now consider a cloud of gas at temperature $T > 0$, absorption by individual atoms yields a single total cross section. Due to the nonzero temperature, the atoms have a thermal velocity v in the radial direction (i.e. along the line of sight), so that although the cross section in their individual rest frames is always given by (3.15), the cross section they contribute to the total cross section of the cloud is centred around a Doppler shifted Ly-α frequency ν'_α, with

$$\nu'_\alpha = \left(1 - \frac{v}{c}\right) \nu_\alpha\,, \tag{3.17}$$

Version of July 8, 2022– Created July 8, 2022 - 21:51

Assuming that $v \ll c$ and that $v > 0$ corresponds to a redshift. The total cross section produced by the cloud is thus the sum of individual contributions (3.15), centred at frequencies shifted according to (3.17) and weighted by the distribution function $f(v)dv$ which describes the fraction of atoms with radial speed in the range $[v, v + dv]$:

$$\sigma_{\text{tot}}(\nu) = \int_{-\infty}^{\infty} \sigma_0 \phi \left(\nu - \left(1 - \frac{v}{c}\right) \nu_0 \right) f(v) dv \, . \tag{3.18}$$

Additionally, we may account for any peculiar velocity of the cloud by shifting the distribution function by the radial peculiar velocity u of the cloud, so $f(v) \to f(v - u)$. To evaluate this expression, we neglect natural and collisional broadening, so the intrinsic line profile is $\phi(\nu - \nu_\alpha) = \delta(\nu - \nu_\alpha)$, a delta function:

$$\begin{aligned} \sigma_{\text{tot}}(\nu) &= \sigma_0 \int_{-\infty}^{\infty} \delta \left(\nu - \left(1 - \frac{v}{c}\right) \nu_\alpha \right) f(v - u) dv \\ &= \sigma_0 \int_{-\infty}^{\infty} \frac{c}{\nu_\alpha} \delta \left(v - \left(1 - \frac{\nu}{\nu_\alpha}\right) c \right) f(v - u) dv \\ &= \sigma_0 \lambda_\alpha f \left(\left(1 - \frac{\nu}{\nu_\alpha}\right) c - u \right) \, , \end{aligned} \tag{3.19}$$

Where $\lambda_\alpha = \frac{c}{\nu_\alpha}$ is the rest frame Ly-α wavelength. To finalise this expression, we assume that the IGM is in thermodynamic equilibrium, and hence $f(v)$ is the one-dimensional Maxwell-Boltzmann distribution, so that

$$\sigma_{\text{tot}}(\nu) = \frac{\sigma_0 \lambda_\alpha}{\sqrt{\pi} b_T} \exp \left(- \left(1 - \frac{\nu}{\nu_\alpha} - \frac{u}{c}\right)^2 \left(\frac{c}{b_T}\right)^2 \right) \, . \tag{3.20}$$

b_T is the thermal velocity defined as

$$b_T^2 \equiv \frac{2 k_B T}{m_{\text{HI}}} \, , \tag{3.21}$$

with m_{HI} the mass of a hydrogen atom. (3.20) may then be substituted for σ in (3.14) to find the actual optical depth; note that both b_T and u will be z-dependent.

3.2.1 Velocity coordinates

Spectrographs usually measure spectra as a function of frequency or wavelength, but their results are often quoted as a function of Doppler velocity. By (3.17), the Doppler effect can be written as

$$v = -\frac{\Delta \nu}{\nu} c \, , \tag{3.22}$$

Where $\Delta\nu$ is the change in frequency of light that was emitted at frequency ν by a source moving at radial speed $|v| \ll c$; the minus sign ensures that $v > 0$ corresponds to a redshift. Taking the limit of infinitesimally separated frequencies yields

$$\begin{aligned} dv &= -\frac{d\nu}{\nu} c \\ v_f &= c \ln \left(\frac{\nu_0}{\nu} \right) \, , \end{aligned} \tag{3.23}$$

Version of July 8, 2022– Created July 8, 2022 - 21:51

With v_f the 'frequency velocity' and ν_0 a normalisation frequency. In principle, ν_0 can be chosen freely, but a reasonable choice is often set by another practical consideration, namely that the optical depth due to the full line of sight is rarely used, but instead τ is calculated along short segments of the full line of sight (these segments will be referred to as LOS). This is done because if a long LOS were used, the LSS would evolve during the time it takes light to traverse the length of the LOS, complicating the way the Ly-α forest produced by such an LOS relates to the LSS. Since σ is, even when accounting for thermal broadening, a relatively sharply peaked function, choosing a short LOS simply corresponds to considering a small segment of the full Ly-α forest.
If the nearest point of an LOS has redshift z_{LOS}, ν_0 can be chosen such that Ly-α emission from this point corresponds to $v_f = 0$:

$$v_f = c \ln\left(\frac{\nu_\alpha}{(1+z_{\mathrm{LOS}})\,\nu}\right) . \tag{3.24}$$

Additionally, if we consider a short LOS, the Hubble parameter does not change much over the time it takes light to travel the length of the LOS and we may parameterise the position along the LOS in velocity coordinates v_r as well. This may be done by considering the infinitesimal version of (2.2), combined with (3.12):

$$dv_r = H(z_{\mathrm{LOS}})dr = \frac{cdz}{1+z} , \tag{3.25}$$

Since $H(z)$ is nearly constant along the LOS. Both equalities may be integrated to yield

$$v_r = H\left(z_{\mathrm{LOS}}\right) r = c \ln\left(\frac{1+z}{1+z_{\mathrm{LOS}}}\right) . \tag{3.26}$$

The integration constants were chosen such that a point at the near end of an LOS has $v_r = 0$ and $r = 0$. By substituting (3.20) into (3.14), expressing the frequencies and redshifts in velocity coordinates using (3.24) and (3.26) and using (3.25) for the coordinate transformation, we obtain the final expression for the optical depth produced by the IGM along a given LOS:

$$\tau(v_f) = \int_{\mathrm{LOS}} \frac{\sigma_0 \lambda_\alpha n_{\mathrm{HI}}(v_r)}{\sqrt{\pi} H(z_{\mathrm{LOS}})} \exp\left(-\left(1 - e^{(v_r - v_f)/c} - \frac{u}{c}\right)^2 \left(\frac{c}{b_T}\right)^2\right) \frac{dv_r}{b_T} . \tag{3.27}$$

Note that both u and b_T depend on the position along the LOS.

3.3 Relation to the dark matter power spectrum

It is clear from (3.27) that the optical depth depends on the distribution of neutral hydrogen, which in turn depends on the total hydrogen distribution through (3.6). Assuming that hydrogen follows the distribution of baryons, the distribution of hydrogen can be related to the dark matter power spectrum using (2.53); ultimately, the statistical properties of the flux $F = e^{-\tau}$ are thus set by the large scale dark matter distribution. This relation is, however, highly non-trivial as several non-linear steps are required and the flux is fundamentally measured along a one-dimensional line of sight, whereas the three-dimensional dark matter power spectrum is required to constrain WDM models. A certain degree of qualitative understanding may be obtained

Version of July 8, 2022– Created July 8, 2022 - 21:51

by considering a highly idealised model, in which the IGM has negligible temperature and peculiar velocities and the baryonic density is very low.
Assuming a stationary IGM allows us to set $u = 0$ in (3.27) and thus rewrite it to

$$\tau\left(v_f\right) = \frac{\sigma_0 \lambda_\alpha}{H\left(z_{\mathrm{LOS}}\right)} \int_{\mathrm{LOS}} n_{\mathrm{HI}}\left(v_f + c\ln\left(1-y\right)\right) \frac{1}{\sqrt{2\pi s^2}} e^{-\frac{y^2}{2s^2}} \frac{dy}{1-y}\,, \tag{3.28}$$

Where $y = 1 - e^{(v_r - v_f)/c}$ and $s = b_T/c\sqrt{2}$. If we now assume a cold IGM, we can take the limit $b_T \to 0$ and hence $s \to 0$, in which case the Gaussian in the integral approximates a delta function:

$$\begin{aligned}\lim_{T\to 0} \tau(v_f) &= \frac{\sigma_0 \lambda_\alpha}{H\left(z_{\mathrm{LOS}}\right)} \int_{\mathrm{LOS}} n_{\mathrm{HI}}\left(v_f + c\ln\left(1-y\right)\right) \delta(y) \frac{dy}{1-y} \\ &= \frac{\sigma_0 \lambda_\alpha}{H\left(z_{\mathrm{LOS}}\right)} n_{\mathrm{HI}}\left(v_f\right) \equiv \frac{n_{\mathrm{HI}}(v_f)}{n_0(z_{\mathrm{LOS}})}\,.\end{aligned} \tag{3.29}$$

Thus, in a stationary and cold IGM, the optical depth is simply a rescaling of the neutral hydrogen density by a reference density $n_0 = \frac{H(z_{\mathrm{LOS}})}{\sigma_0 \lambda_\alpha}$. At $z = 0$, combining (3.16) with $H_0 = 67.66\,\mathrm{km/s/Mpc}$ [11] yields $n_0 \approx 1.77 \times 10^{-5}\ \mathrm{m}^{-3}$. If we assume that $\tau(v_f) \ll 1$ (due to $n_{\mathrm{HI}} \ll n_0$), the flux F can be directly related to n_{HI}:

$$F(v_f) = e^{-\tau(v_f)} \approx 1 - \tau(v_f) = 1 - \frac{n_{\mathrm{HI}}\left(v_f\right)}{n_0\left(z_{\mathrm{LOS}}\right)}\,. \tag{3.30}$$

We can now define, analogously to the density contrast, the flux contrast as

$$\delta_F(v_f) = \frac{F(v_f)}{\langle F\rangle} - 1\,, \tag{3.31}$$

Where the average is calculated over many LOS at the same redshift. Thus, we can relate the flux contrast to the density contrast in the neutral hydrogen as

$$\begin{aligned}\delta_F(v_f) &= \frac{1 - \frac{n_{\mathrm{HI}}(v_f)}{n_0(z_{\mathrm{LOS}})}}{1 - \frac{\langle n_{\mathrm{HI}}\rangle}{n_0(z_{\mathrm{LOS}})}} - 1 \\ &\approx \frac{\langle n_{\mathrm{HI}}\rangle}{n_0\left(z_{\mathrm{LOS}}\right)} \frac{\langle n_{\mathrm{HI}}\rangle - n_{\mathrm{HI}}(v_f)}{\langle n_{\mathrm{HI}}\rangle} \\ &= -\frac{\langle n_{\mathrm{HI}}\rangle}{n_0\left(z_{\mathrm{LOS}}\right)} \delta_{\mathrm{HI}}\,,\end{aligned} \tag{3.32}$$

Where $\langle n_{\mathrm{HI}}\rangle$ is the average neutral hydrogen density along the LOS and δ_{HI} is the neutral hydrogen density contrast. We may now define the one-dimensional Fourier transform as

$$\delta_F(k_v) = \int_0^{V_{\mathrm{LOS}}} \delta_F(v) e^{-ik_v v} dv\,, \tag{3.33}$$

Where the LOS has length V_{LOS} when expressed in velocity coordinates. Additionally, we may define the flux power spectrum (FPS) and the dimensionless FPS (also often referred to as the FPS) in analogy to (2.23) and (2.24) as

$$\Delta_F^2(k_v) \equiv \frac{k_v}{\pi} P_F(k_v) = \frac{k_v}{\pi} \frac{\langle |\delta_F(k_v)|^2\rangle}{V_{\mathrm{LOS}}}\,. \tag{3.34}$$

Thus, in this model we may relate the FPS and the one-dimensional power spectrum of neutral hydrogen as

$$P_F(k_v) = \frac{\langle n_{\mathrm{HI}} \rangle^2}{n_0^2\,(z_{\mathrm{LOS}})} P_{\mathrm{HI},1D}(k_v)\ . \tag{3.35}$$

We may relate this one-dimensional power spectrum to the three dimensional neutral hydrogen power spectrum using

$$P_{\mathrm{HI},3D}(k_v) = -\frac{2\pi}{k_v}\frac{dP_{\mathrm{HI},1D}}{dk_v}\ , \tag{3.36}$$

Which can be proven under the assumption that δ_{HI} follows a homogeneous and isotropic random distribution. If we assume that, due to the low temperature and hence high recombination rate, all hydrogen is neutral, we thus see that

$$P_H(k_v) = -\frac{2\pi}{k_v}\frac{n_0^2\,(z_{\mathrm{LOS}})}{\langle n_H \rangle^2}\frac{dP_F}{dk_v}\ . \tag{3.37}$$

Finally, (2.53) can then be used to find the dark matter power spectrum.
This treatment is of course unrealistic in several ways: there are peculiar velocity fields in the IGM (see section 2.3.3), the IGM has a quite significant temperature [19], and finally the density n_0 is low enough that often the assumption $n_{\mathrm{HI}} \ll n_0$ will not hold. However, several qualitative remarks can be made based on this treatment. For example, even in a realistic model a peak n_{HI} will correspond to a peak in the optical depth (or a dip in the flux), at a frequency corresponding to v_r but shifted by the peculiar velocity. Also, the definitions (3.31) and (3.34) are used to describe the statistical properties of the Ly-α forest because even if they are difficult to relate quantitatively to the (dark) matter power spectrum, they share qualitative properties. For example, a cutoff present in the power spectrum of dark or baryonic matter will produce a similar cutoff in the FPS.
In short, the FPS differs from the true dark matter power spectrum in several ways:

1. The FPS is measured along a one-dimensional LOS.
2. The flux F and the neutral hydrogen density n_{HI} are non-linearly related.
3. The neutral fraction is temperature-dependent, which by (3.7) means it is density-dependent.
4. The flux is influenced by thermal broadening and peculiar velocities.
5. There is a pressure cutoff in the FPS relative to the dark matter power spectrum.

Because of these complications, exacerbated by the fact that the thermal history of the IGM is not very well constrained, it is often impossible to reconstruct the dark matter power spectrum from the FPS. Instead, modern approaches use numerical methods to simulate the density field under the assumption of a certain cosmological model, after which the FPS can be calculated and compared to the observed FPS. This thesis follows a similar path to assess the influence of peculiar velocities on the FPS, using simulations and numerical methods introduced in the next chapter.

Version of July 8, 2022– Created July 8, 2022 - 21:51

3.4 Modelling a characteristic scale for the influence of peculiar velocities

Motivated by the preceding discussion, which stated that a density feature at position v_r will create a spectral feature at frequency $v_r - u$, we propose that a characteristic scale Δv may be associated to the influence of peculiar velocities. To see why this might be the case, consider an isolated peak in the density. According to (2.58), there will be a peculiar velocity field associated with this density peak, such that the peculiar velocity $\mathbf{u}$ is directed towards the minimum of the potential, or equivalently through (2.40) the maximum of the density. Hence, matter that is closer to the observer than the density peak will produce an absorption feature that is redshifted (since it is moving towards the density peak and hence away from the observer), while matter that is beyond the density peak will produce a blueshifted absorption feature. Therefore, the spectral feature produced by the entire density peak will be more narrow with peculiar velocities than it would have been without. Since peculiar velocities cannot be arbitrarily high and very small peculiar velocities have negligible impacts, there may be some peculiar speed that has both a significant influence and is well-represented in the peculiar velocity field. This scale then corresponds to Δv.
In order to obtain a crude model of the dependency of Δv on the properties of the IGM, consider a Gaussian density peak in n_{HI} of width σ around some position μ along a LOS. If we assume a negligible temperature, the optical depth profile without peculiar velocities will also be a Gaussian due to (3.29). This optical depth can be written as

$$\tau(v_f) = \frac{\tau_0}{\sqrt{2\pi\sigma^2}} e^{-\left(\frac{v_f-\mu}{\sigma}\right)^2}, \tag{3.38}$$

Where τ_0 is related to the average optical depth along the LOS. In fact, based on (3.29), it may be proportional to the neutral hydrogen density, which in turn is set by (3.6). Since the flux is exponentially related to the optical depth, all optical depths higher than some limiting value τ_{lim} (for example 5) will produce a negligible flux; the width of the absorption feature produced by this density peak is thus set by the range of frequencies for which $\tau(v_f) \geq \tau_{\mathrm{lim}}$. For the Gaussian density peak, the lowest frequency for which equality occurs is given by

$$v_1 = \mu - \sigma\sqrt{2\ln\left(\frac{\tau_0}{2\tau_{\mathrm{lim}}\sqrt{2\pi\sigma^2}}\right)}. \tag{3.39}$$

As argued before, peculiar velocities narrow down absorption features[2]; hence, the addition of peculiar velocities changes σ to $\sigma' < \sigma$. The magnitude of the difference depends on the magnitude of the peculiar velocities, and hence the typical difference depends on the typical peculiar speed which we may characterise with the root mean square (RMS) peculiar velocity

$$\sigma_u = \sqrt{\langle u^2 \rangle}. \tag{3.40}$$

[2]Strictly speaking, peculiar velocities may also change the shape of the absorption feature since the peculiar velocities depend non-linearly on the density. We will ignore this effect.

Version of July 8, 2022– Created July 8, 2022 - 21:51

σ_u is also known as the velocity dispersion. Then, to first order we may approximate

$$\sigma'(\sigma_u) \approx \sigma + \frac{\partial \sigma'}{\partial \sigma_u}\sigma_u = \sigma - A\sigma_u \,, \tag{3.41}$$

Where A is some constant factor. Thus, peculiar velocities change v_1 to v_1' by modifying σ to σ'; if we neglect the dependence of the logarithm on σ (since it is not only logarithmic but also taken the square root of, as opposed to the linear dependence of the prefactor), the result is a shift

$$\Delta v = v_1' - v_1 \approx A\sigma_u \sqrt{2\ln\left(\frac{\tau_0}{2\tau_{\text{lim}}\sqrt{2\pi\tilde{\sigma}^2}}\right)} \,, \tag{3.42}$$

With $\sigma' < \tilde{\sigma} < \sigma$ some effective width. As noted before, τ_0 may be proportional to the typical neutral hydrogen density which can be found through (3.6) at $T = T_0$ and $\delta_H = 0$. Indeed, inspired by (3.29), we may propose that τ_0 is proportional to the typical optical depth in a completely cold[3] and static IGM and summarise all other dependencies (from τ_{lim}, $\tilde{\sigma}$ and factors depending on the inhomogeneity of the density field) in a constant parameter B, and hence we can propose

$$\Delta v = A\sigma_u \sqrt{2\ln\left(B\frac{\langle n_H\rangle^2}{n_0(z_{\text{LOS}})}\frac{\alpha_{\text{HII}}(T_0)}{\Gamma_{\text{HI}}}\right)} \,. \tag{3.43}$$

Both A and in particular B may be redshift dependent as structure forms and the peculiar velocity field evolves. Note that (3.43) contains no explicit reference to the width of the density peak; hence, we expect it to be independent of thermal broadening.
The Δv as defined in (3.43) is thus a typical scale on which peculiar velocities broaden absorption features in the Ly-α forest. Hence, if there is any systematic impact of these peculiar velocities on the FPS, we expect it to have Δv as typical scale.

[3] Although the recombination rate is still set by $T_0 > 0$.

Chapter 4

Simulations and methods

As described in the previous chapter, one of the ways in which the flux power spectrum of the Ly-α forest (henceforth the FPS) differs from the dark matter power spectrum is the influence of peculiar velocity fields. These velocities are irrelevant for the dark matter power spectrum[1], but they influence the FPS because they cause Doppler shifts in the absorption features that constitute the Ly-α forest. In this thesis we attempted to quantify this influence. To do so, simulations of the cosmic density field were obtained and used to calculate the FPS while ignoring or incorporating the peculiar velocities.
This chapter will first briefly introduce the simulations used for this investigation and then describe the numerical methods used to first calculate the FPS and then quantify the difference between the cases including or neglecting the peculiar velocities.

4.1 The SWIFT simulation

The simulations used in this thesis were performed using the SWIFT (SPH With Interdependent Fine-grained Tasking) code, which is extensively described in [44] and at https://swift.dur.ac.uk/. In short, SWIFT is a simulation code which evolves discrete particles under the influence of gravity and pressure and then uses the particle distribution to interpolate the hydrodynamical state (i.e. density, pressure and velocity) to cells on a regular grid. This procedure is called Smoothed Particle Hydrodynamics, abbreviated to SPH (for a review on this technique, see for example [45]). Specifically, SWIFT identifies two types of tasks related to the interpolation: calculating the contribution to the density in a cell by the particles within that cell and calculating the contribution to the density in a cell by particles in adjacent cells (the cell size is chosen such that particles can only contribute to the cells adjacent to their own cell). Crucially, every cell can only be used for a single task at a time, and SWIFT distinguishes itself from other codes by explicitly organising the tasks in such a way that a maximum amount of tasks can be performed in parallel. This speeds up calculations significantly [44] and thus allows SWIFT to perform high-resolution simulations relatively quickly.

[1] Although they are essential for the evolution of this power spectrum, see section 2.3.3.

Version of July 8, 2022– Created July 8, 2022 - 21:51

Table 4.1: *Cosmological parameters used in* `SWIFT` *and literature values for these parameters; the literature value of the hydrogen mass fraction Y_H assumes that contributions from elements other than hydrogen and helium are negligible.*

Cosmological parameter	`SWIFT` value	Literature value
H_0	$67.77\,\mathrm{km\,s^{-1}\,Mpc^{-1}}$	$67.66 \pm 0.42\,\mathrm{km\,s^{-1}\,Mpc^{-1}}$ [11]
Ω_m	0.307	0.3111 ± 0.0056 [11]
Ω_Λ	0.693	0.6889 ± 0.0056 [11]
Ω_b	0.0482519	0.04897 ± 0.00068 [11]
Y_H	0.7600	$0.7564^{+0.0039}_{-0.0040}$ [46]

The simulations used in this thesis were performed in a periodic volume of comoving size 25 Mpc, with the cosmological parameters given in table 4.1. The spatial resolution was $1.4\,\mathrm{km\,s^{-1}}$, and the number of particles was approximately 250^3 although the exact number decreased slightly with time (by approximately 5% over the redshift range considered here). The density field was evolved from redshift $z = 12.0$ to $z = 2.1$; here we used redshifts $4.0 \leq z \leq 6.0$, with snapshots obtained at redshifts separated by $\Delta z = 0.5$. Within each simulation snapshot, 500 lines of sight (LOS) along one of the coordinate axes along the entire box length were obtained using the `SpecWizard` code, yielding the density contrast of all hydrogen (i.e. both ionised and neutral), peculiar velocities and coordinates in velocity units along the LOS. Furthermore, the `SWIFT` code also simulated the coefficients T_0 and γ from (3.7).

4.2 Determining the flux power spectrum

The simulation snapshots yielded the density contrast δ_H in all hydrogen. n_H, the total hydrogen number density, was thus obtained as

$$n_H = Y_H \Omega_b \frac{3H_0^2}{8\pi G m_H} \left(1 + z_{\mathrm{LOS}}\right)^3 \left(1 + \delta_H\right) \ , \tag{4.1}$$

With Y_H the mass fraction of hydrogen, $G = 6.674 \times 10^{-11}\ \mathrm{m^3\,kg^{-1}\,s^{-2}}$ the gravitational constant, z_{LOS} the redshift of the simulation snapshot and m_H the mass of a hydrogen atom[2]. The temperature was calculated as

$$T = T_0 \left(1 + \delta_H\right)^{\gamma - 1} \ . \tag{4.2}$$

With both the temperature and the total hydrogen density now known, the neutral hydrogen density could be calculated through (3.6), with models for Γ_{HI} and α_{HII} taken from [39] and [43], respectively. Finally, since both z_{LOS} and the comoving box size $L = 25\,\mathrm{Mpc}$ were known and the length V_{LOS} of the box in velocity units was given, the Hubble parameter at the snapshot redshift could be calculated as

$$H(z_{\mathrm{LOS}}) = \frac{V_{\mathrm{LOS}}}{L/(1 + z_{\mathrm{LOS}})} \ . \tag{4.3}$$

[2]Strictly speaking, since hydrogen is mostly ionised, a weighted average of the proton and hydrogen mass would have been more appropriate. However, because the electron mass is negligible with respect to the proton mass, any discrepancies caused by the mass difference between a proton and a hydrogen atom should be negligible as well.

Version of July 8, 2022– Created July 8, 2022 - 21:51

With this, (3.27) could be evaluated to obtain the optical depth, which was done at twice the spatial resolution of the LOS to prevent aliasing when taking the Fourier transform. Furthermore, an additional margin in the evaluated frequencies equal to 7.5% more than the maximum peculiar velocity was taken into account; because the simulation volume was assumed to be periodic, any optical depth at $v_f < 0$ could be added to the optical depth at the high-frequency end of the spectrum, and any optical depth at $v_f > V_{\text{LOS}}$ could be added to the low-frequency end. (3.27) was evaluated twice for each LOS; once with the peculiar velocities u as taken from the simulation snapshot and once with $u = 0$.
From the optical depths thus calculated, a flux F could be calculated using (3.10), yielding 500 Ly-α forest spectra, one along each LOS. Using (3.31) with the average over all LOS, the flux was converted to a flux contrast, which was then numerically Fourier transformed according to (3.33), and finally squared and averaged to obtain the FPS as in (3.34). Error margins on Δ_F^2 at each k_v were estimated using the variance on the values of $|\delta_F(k_v)|^2$ for the different LOS. Since this assumes that the error on Δ_F^2 is dominated by statistical and not systematic errors (such as cosmic variance, in which a simulation volume is statistically different from the universe as a whole), the calculated FPS was compared to observations from [47] of the Ly-α FPS to ascertain that our calculations yielded reasonable results. As these observations do not probe scales smaller than $k_v = 0.1\,\text{s km}^{-1}$, the analysis performed in this thesis has been limited to $k_v \leq 0.3\,\text{s km}^{-1}$. Similarly, current observations only accurately probe scales with $\Delta_F^2 \gtrsim 10^{-3}$, and hence our analysis has been limited to k_v for which $\Delta_F^2(k_v) \geq 10^{-3}$ in both the scenario with and without peculiar velocities.

4.3 Extracting the characteristic scale

As motivated in section 3.4, peculiar velocities tend to make peaks in the optical depth, and thus through (3.10) absorption features in the flux, more narrow. In the case that the Ly-α forest is dominated by absorption and therefore only displays several transmission features, this may equally well be interpreted as a broadening of these transmission features. That this is a valid interpretation is demonstrated by figure 4.1, which shows an example Ly-α forest at $z = 4.0$ and clearly demonstrates transmission features being broadened (and shifted) due to the peculiar velocities.
We may now draw an analogy to the effect of pressure on the baryonic power spectrum, since pressure also broadens structures of baryonic matter with respect to the underlying dark matter structure. Hence, if the Ly-α forest is dominated by absorption, we may expect peculiar velocities to introduce a Gaussian cutoff to the FPS in analogy to (2.53), with cutoff scale k_0. Assuming that the peculiar velocities leave the FPS otherwise unchanged, this Gaussian cutoff should become apparent in a quantity $\mathcal{D}$ defined as

$$\mathcal{D}(k_v) = \frac{\Delta^2_{F,\,\text{with u}}(k_v)}{\Delta^2_{F,\,\text{without u}}(k_v)} - 1\,. \tag{4.4}$$

$\mathcal{D}$ is the fractional deviation between the FPS with peculiar velocities $\Delta^2_{F,\,\text{with u}}$ and without peculiar velocities $\Delta^2_{F,\,\text{without u}}$, chosen such that $\mathcal{D} < 0$ corresponds to a suppression of the FPS. Error margins on $\mathcal{D}$ were obtained by propagating the errors on the respective FPS.

Version of July 8, 2022– Created July 8, 2022 - 21:51

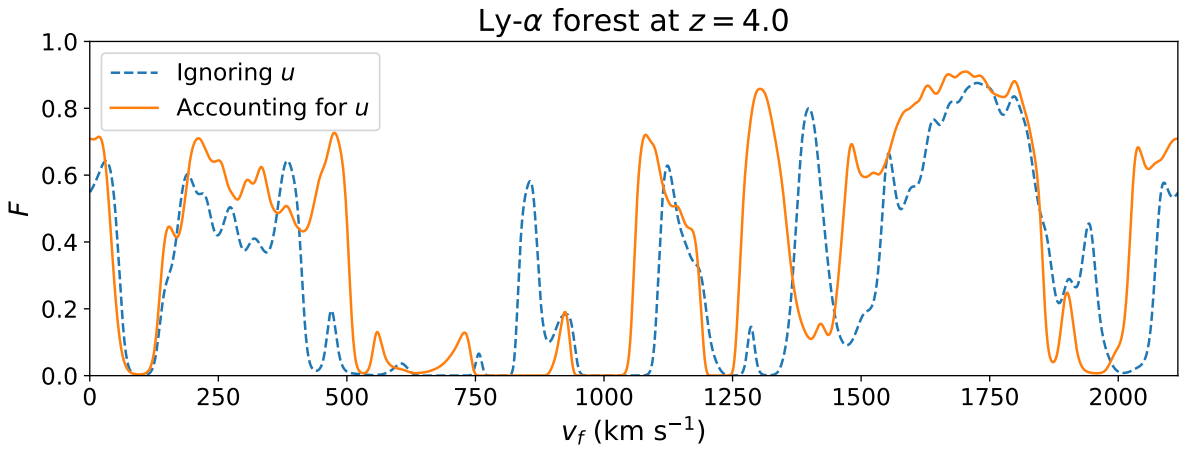

Figure 4.1: *An example of the Ly-α forest at $z = 4.0$, showing the flux F as a function of frequency v_f. The solid orange curve shows the flux when accounting for peculiar velocities, while the dashed blue one demonstrates the flux when ignoring peculiar velocities. Qualitatively, the shapes of the two spectra are similar, but the transmission features in the spectrum with peculiar velocities appear noticeably shifted (e.g. the tallest peak between* $1250\,\mathrm{km\,s^{-1}}$ *and* $1500\,\mathrm{km\,s^{-1}}$*) and broadened (e.g. the main feature between* $1000\,\mathrm{km\,s^{-1}}$ *and* $1250\,\mathrm{km\,s^{-1}}$*).*

k_0 can be related to the characteristic scale Δv introduced in (3.43) by supposing that k_0 is the wavenumber with spatial scale Δv, so that $k_0 = \frac{2\pi}{\Delta v}$ and for a Gaussian cutoff

$$\mathcal{D}(k_v) = \mathcal{D}_0 \exp\left(-\frac{1}{2}\left(\frac{k_v \Delta v}{\pi}\right)^2\right) - 1\,, \tag{4.5}$$

With $\mathcal{D}_0 \sim 1$ an amplitude. (4.5) could then be fitted to the $\mathcal{D}$ as calculated from the FPS using a least-squares fit. In this fitting procedure, the reduced χ^2 is defined as

$$\chi^2_{\mathrm{red}}(\mathcal{D}_0, \Delta v) = \frac{1}{n}\sum_i \left(\frac{\mathcal{D}(k_{v,\,i}) - \mathcal{D}_m\left(k_{v,\,i}, \mathcal{D}_0, \Delta v\right)}{\sigma_{\mathcal{D},\,i}}\right)^2 \pm \sqrt{\frac{2}{n}}\,. \tag{4.6}$$

The summation is done over all relevant data points, indexed i. $k_{v,\,i}$ are then the k_v of the relevant data points $\mathcal{D}\left(k_{v,\,i}\right)$, which have error margins $\sigma_{\mathcal{D},\,i}$, and $\mathcal{D}_m$ is the value of $\mathcal{D}$ assuming (4.5) and a set of parameters $(\mathcal{D}_0, \Delta v)$. The error is estimated using the number of degrees of freedom n, equal to the number of points minus the number of fitted parameters, under the assumption that $n \gg 1$. The least-squares fit then finds parameters that minimise (4.6), and we reject the Gaussian model as a good description of $\mathcal{D}$ if the minimal χ^2_{red} is more than 2σ above 1. A fit that is not rejected on this criterion is said to pass the χ^2-test.
As can be seen from figure 4.2, a Gaussian cutoff can describe $\mathcal{D}$ properly at low k_v. However, at high k_v there is a clear trend reversal and $\mathcal{D}$ increases again, eventually even indicating that the FPS is enhanced by peculiar velocities ($\mathcal{D} > 0$). We may refer to this small-scale effect as a 'recovery effect', as power is recovered relative to the suppression by peculiar velocities at low k_v. We postpone a discussion of the cause of this recovery effect to chapter 6, and merely note that to fit a Gaussian to $\mathcal{D}$, a range of k_v in which $\mathcal{D}$ is relatively unaffected by the recovery effect had to be used. We defined this range as all k_v that are at most 60% of the k_v at which $\mathcal{D}$ is minimised, with 60% chosen as the maximum fraction that still yielded visually acceptable fits.

Version of July 8, 2022– Created July 8, 2022 - 21:51

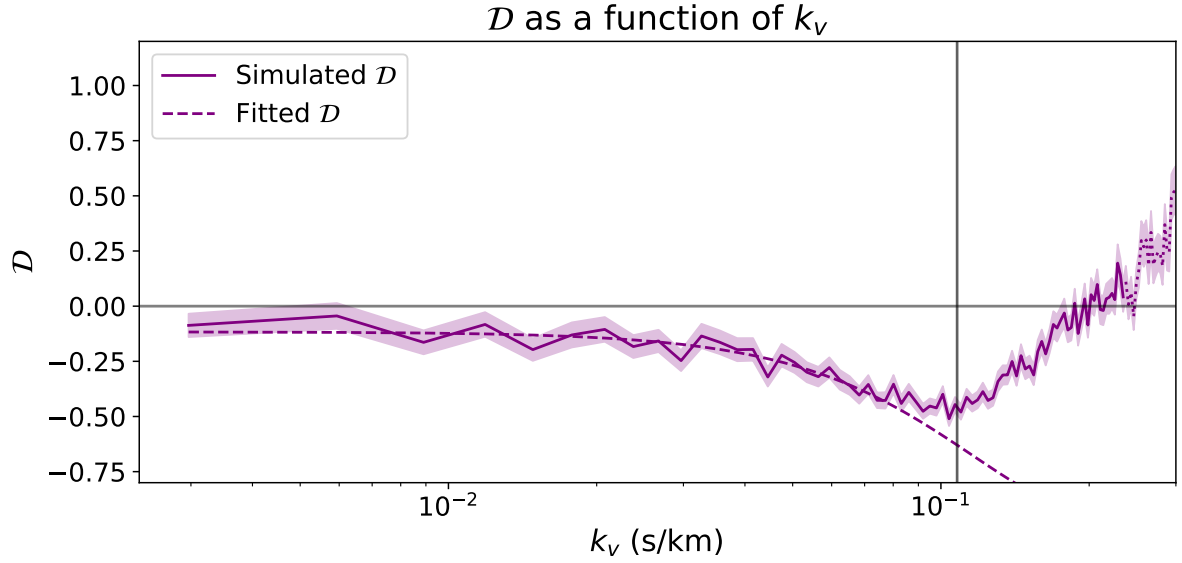

Figure 4.2: *An example at $z = 4.0$ of the influence of peculiar velocities on the FPS. This figure shows $\mathcal{D}$ calculated from the FPS at $z = 4.0$, in turn calculated with the regular, simulated T_0, γ, σ_u and $\langle n_H \rangle$, the mean total hydrogen number density; $\mathcal{D}$ is shown as a solid curve, with error margins indicated with a shaded region. The dotted part corresponds to the range of k_v in which Δ_F^2 with or without peculiar velocities is less than the observability limit 10^{-3}. The solid vertical line is drawn at $k_v = 2\pi/\sigma_u$, the k_v corresponding to the peculiar velocity dispersion at $z = 4.0$. The dashed curve shows the best fitting Gaussian for the $\mathcal{D}$ at values of k_v that are at most 60% of the k_v at which $\mathcal{D}$ is minimised.*

The exact definition of the minimum of $\mathcal{D}$ is less straightforward than could be expected based on figure 4.2, as this figure presents a $\mathcal{D}$ that does not stop increasing once it begins to. However, the strength of the recovery effect varies between different FPS, and hence it may be that $\mathcal{D}$ does not recover but merely stabilises; the absolute minimum of $\mathcal{D}$ may then be noise-induced, such that even a range of k_v up to 60% of the k_v of this absolute minimum extends well into the range of k_v in which the recovery effect dominates. To prevent this from occurring, we calculated the average $\mathcal{D}$ in the range[3] $\frac{2\pi}{\sigma_u} \leq k_v \leq 0.3\,\mathrm{s\,km^{-1}}$, weighted by the inverse variance of each $\mathcal{D}$. Then, χ^2_{red} was calculated analogously to (4.6). $\mathcal{D}$ was considered constant if this constant fit had a minimal χ^2_{red} that was at most 0.5σ above 1, since this implied that a constant fit was not just acceptable but with near certainty optimal[4]. If $\mathcal{D}$ was indeed constant for $\frac{2\pi}{\sigma_u} \leq k_v \leq 0.3\,\mathrm{s\,km^{-1}}$, we defined the minimum of $\mathcal{D}$ as the absolute minimum for $k_v \leq \frac{2\pi}{\sigma_u}$; if it was not constant, the minimum of $\mathcal{D}$ was defined as the first local minimum with respect to at least 30 neighbouring data points.
As mentioned before, a Gaussian cutoff was rejected as a good description of $\mathcal{D}$ if the minimal χ^2_{red} was more than 2σ above 1. By restricting the range of k_v used for fitting, we introduced two new grounds for rejection. Firstly, all fits based on 10 or fewer data points were rejected, as many curves can be successfully fitted to so little data. Sec-

[3]The lower limit was chosen to be equal to the k_v corresponding to the peculiar velocity dispersion σ_u, since figure 4.2 indicates that the recovery effect typically dominates at scales smaller than σ_u.

[4]Note that the Gaussian fit was rejected if χ^2_{red} was more than 2σ above 1, while the constant fit was accepted if χ^2_{red} was less than 0.5σ above 1. The difference is that the Gaussian fit had to be acceptable, but a constant $\mathcal{D}$ was demanded to be nearly optimal.

Version of July 8, 2022– Created July 8, 2022 - 21:51

ondly, the Gaussian fit was also rejected if the fitted $\Delta v < 2.09\,\mathrm{km\,s^{-1}}$, which is equal to one tenth of the minimum scale probed for $k_v \leq 0.3\,\mathrm{s\,km^{-1}}$. The reasoning behind this rejection is that such a small cutoff essentially yields a constant $\mathcal{D}_m$ within the considered range of k_v and thus cannot be used for a statistically significant determination of Δv (indeed, if a cutoff is present at all). A final and separate ground for rejection was taken to be $\langle F \rangle < 0.005$ without peculiar velocities, as this implied that the fit to $\mathcal{D}$ was ultimately based on nearly vanishing amounts of flux, which we deemed to be too unreliable.
We have used the Python package `scipy.optimize` to perform the least-squares fitting; error margins on the fitted parameters are extracted from the diagonal of the estimated covariance matrix.

4.4 Extracting the dependencies of Δv

In this way, a value of Δv could be obtained for a given calculation of the FPS. Section 3.4 introduced a model to describe Δv, namely as a function of the thermal scale T_0, peculiar velocity dispersion σ_u and average total hydrogen density $\langle n_H \rangle$:

$$\Delta v = A\sigma_u \sqrt{2 \ln\left(B \frac{\langle n_H \rangle^2}{n_0(z_{\mathrm{LOS}})} \frac{\alpha_{\mathrm{HII}}(T_0)}{\Gamma_{\mathrm{HI}}} \right)} \,. \tag{4.7}$$

To test whether Δv is properly described by (4.7), Δv was calculated from the FPS calculated with different $\langle n_H \rangle$, T_0, σ_u or amounts of thermal broadening, keeping all other parameters constant at their originally simulated value. For $\langle n_H \rangle$ this meant multiplying n_H as obtained through (4.1) by a constant factor, while T_0 could be set to a different value than simulated and be used consistently afterwards. This means that varying T_0 strictly speaking varied both the ionisation fraction and the degree of thermal broadening; we will refer to this as the temperature dependency of Δv. To rescale σ_u, all peculiar velocities were multiplied by a constant value as

$$u = u_{\mathrm{sim}} \frac{\sigma_u}{\sigma_{u,\,\mathrm{sim}}} \,, \tag{4.8}$$

With u_{sim} the simulated peculiar velocities with velocity dispersion $\sigma_{u,\,\mathrm{sim}}$, and u the peculiar velocities rescaled to have velocity dispersion σ_u. Finally, the degree of thermal broadening was varied by using the neutral hydrogen densities as provided by the simulation (instead of using (3.6)) and then varying T_0; this way, T_0 only contributed to the FPS through the thermal broadening in (3.27).
(4.7) could then be fitted to the values of Δv thus obtained using a least-squares fit by minimising $\chi^2_{\mathrm{red}}(A, B)$ calculated in analogy to (4.6). (4.7) could be fitted to Δv as a function of $\langle n_H \rangle$ or as a function of T_0 independently, yielding independent estimates of A and B. These were then respectively averaged, weighted by their inverse variance, to obtain a final estimate of A and B. To judge whether these values, combined with (4.7), yielded an acceptable description of Δv, the following reduced χ^2 was calculated in analogy to (4.6):

$$\chi^2_{\mathrm{red}} = \frac{1}{n} \sum_i \left(\frac{\Delta v_{\mathrm{mod}}(x_i) - \Delta v_{\mathrm{sim}}(x_i)}{\sigma_{\mathrm{sim},\,i}} \right)^2 \pm \sqrt{\frac{2}{n}} \,. \tag{4.9}$$

Version of July 8, 2022– Created July 8, 2022 - 21:51

The summation is over all different values of the independent variable x (which may be $\langle n_H \rangle$ or T_0), Δv_{mod} is the cutoff scale predicted by (4.7), and Δv_{sim} is the cutoff scale from the simulations, with error σ_{sim}; n is the number of degrees of freedom, given by the number of values of Δv being used for fitting minus the number of fitted parameters. Similarly as in section 4.3, we rejected (4.7) as a model for Δv if the minimal χ^2_{red} was more than 2σ above 1; if (4.7) was not rejected on this basis, we say that it has passed the χ^2-test.
The values Δv for different σ_u were used to yield an estimate for

$$C = \frac{\Delta v}{\sigma_u} = A\sqrt{2\ln\left(B\frac{\langle n_H\rangle^2}{n_0(z_{\mathrm{LOS}})}\frac{\alpha_{\mathrm{HII}}(T_0)}{\Gamma_{\mathrm{HI}}}\right)}\,, \tag{4.10}$$

For the simulated values of $\langle n_H \rangle$ and T_0. This was done by dividing each Δv by its corresponding σ_u and taking the average of the results, weighted by the inverse variances on Δv. The value of C thus obtained could be compared to the one calculated using the best estimates for A and B to check the consistency of (4.7) as a model. Furthermore, a χ^2_{red} could be calculated through (4.9), now with $x = \sigma_u$ and $\Delta v_{\mathrm{mod}}(x, C) = C\sigma_u$. Again, this fit was rejected if it did not pass the χ^2-test. Finally, to judge whether Δv is truly independent of thermal broadening, the values of Δv for different degrees of thermal broadening were compared to their average, weighted by their inverse variance. The quality of this fit was then judged based on a χ^2-test with the analogous expression for (4.9), so with Δv_{mod} the weighted average.
The range of independent variables was set as follows: $\langle n_H \rangle$ was allowed to vary between the values of (4.1) with z_{LOS} ranging from 2.0 to 7.0; T_0 was varied from 500 K up to 50 000 K and σ_u was varied from 5 km s^{-1} up to 100 km s^{-1}.

4.5 Checking the effects of finite resolution

Since the research in this thesis is mainly based on simulations with finite resolution, numerical artefacts might arise, influencing the FPS in unphysical ways. Since the simulations used in this thesis have very high spatial resolution and we restricted our consideration to small values of k_v, this was not expected to be a significant effect. To ascertain the validity of this expectation, we calculated several curves of $\mathcal{D}$ (using the simulated, regular parameters at different redshifts) and then repeated this calculation but with a lower physical resolution. To achieve this lower resolution, subsequent pairs of data points (i.e. of the peculiar velocity u and the density contrast δ_H) were averaged, effectively yielding a simulation with half the resolution of the actual simulation. Then, the difference between $\mathcal{D}$ calculated with the standard resolution and with the lowered resolution was calculated[5]; if the effects described here are indeed not due to numerical artefacts, this difference should always be insignificantly different from 0.

[5]The rationale behind using the difference between different calculations of $\mathcal{D}$ instead of the FPS itself is that the cutoff is fitted to $\mathcal{D}$, which is therefore the most critical data set. Furthermore, we use the difference instead of the ratio because all $\mathcal{D}$ are roughly of the same order of magnitude.

4.6 Summary of methods

For quick reference, we present a brief summary of the method employed in this thesis as follows:

1. In a given simulation snapshot, we calculated the optical depths along all LOS using (3.27), with and without peculiar velocities.
2. Using the optical depths, we calculated the flux (contrast) and converted to the FPS through (3.34).
3. We calculated $\mathcal{D}$ as defined in (4.4) and fit (4.5) to the large-scale range of k_v to obtain Δv.
4. This was repeated with different $\langle n_H \rangle$, T_0, σ_u, and amounts of thermal broadening.
5. We fitted (4.7) to the resulting Δv as function of $\langle n_H \rangle$ and as a function of T_0 to obtain two independent estimates of A and B.
6. To obtain final estimates of A and B, we took the weighted average of their values as fitted to Δv as a function of $\langle n_H \rangle$ and as a function of T_0. We then judged whether the model (4.7) was successful using (4.9) and the difference between the minimal χ^2_{red} and 1, which could not exceed 2σ.
7. We compared the value of C as calculated directly from the dependence of Δv on σ_u through the first equality of (4.10) to the value of C predicted from A and B through the second equality of (4.10).
8. The directly proportional fit $\Delta v = C\sigma_u$ was tested through the analogous expression of (4.9) and the difference between the minimal χ^2_{red} and 1, which should not exceed 2σ.
9. We tested the independence of Δv from thermal broadening by comparing Δv as a function of thermal broadening to the average, weighted by the variance; we rejected independence if a constant Δv did not pass the χ^2-test.
10. This was repeated for redshifts $z = 4.0$, $z = 4.5$, $z = 5.0$, $z = 5.5$ and $z = 6.0$.

Version of July 8, 2022– Created July 8, 2022 - 21:51

Chapter 5

Results

The eventual goal of this thesis is to demonstrate that a small-k_v Gaussian cutoff (4.5) may be an acceptable model for the impact of peculiar velocities, and that the cutoff scale can be consistently described reasonably well by (3.43). Finally, we intend to find the redshift dependence of the A and B parameters of (3.43).
To achieve these goals, this chapter will show the results of the methods of chapter 4. We show the dependency of Δv on $\langle n_H \rangle$, T_0, σ_u and thermal broadening at five redshifts ranging from $z = 4.0$ to $z = 6.0$, explicitly noting why Gaussian fits were rejected. After fitting (3.43) to the resulting dependencies of Δv, the quality of the fit and the internal consistency of A, B and C (as defined in (4.10)) will be briefly discussed. Finally, we show how A and B evolve with redshift and consider the relative importance of the peculiar velocity induced cutoff with regard to the pressure and thermal broadening cutoffs.
The test for consistency between the simulated flux power spectrum (FPS) and an empirical measurement of the FPS is performed in appendix A; we note that there is relatively good agreement. Finally, the test for numerical artefacts is performed in appendix B; we remark here that there is no indication of any of the effects discussed here being due to numerical artefacts.

5.1 Overview of figure symbols

In this chapter, we will show the cutoff scale as obtained from both successful and failed fits of a Gaussian cutoff to $\mathcal{D}$. However, as described in section 4.3, there are many grounds to reject a Gaussian fit. For convenience and brevity, we provide an overview of the symbols used in subsequent plots to represent Δv in accepted Gaussian fits and the various rejected Gaussian fits.

1. *Green circles* are used to represent Δv as obtained from successful fits of a Gaussian cutoff to $\mathcal{D}$.
2. *Red squares* represent Δv as obtained from fits were rejected because the Gaussian fit did not pass the χ^2-test (i.e. it had χ^2_{red} more than 2σ above 1).
3. *Light-blue diamonds* represent Δv from fits that are based on 10 or less data points and are thus considered unreliable.

4. *Purple crosses* represent cases in which no cutoff was detected at all because $\mathcal{D}$ was immediately dominated by the recovery effect.
5. *Grey pentagons* represent Δv as obtained from an otherwise successful Gaussian fit that was excluded from subsequent analysis nonetheless because the Ly-α forests it was based on had $\langle F \rangle \leq 0.005$ without peculiar velocities.
6. *Narrow dark-blue diamonds* represent $\Delta v \leq 2.09\,\mathrm{km\,s^{-1}}$, which were rejected because such a cutoff scale yields a basically constant $\mathcal{D}$ at scales $k_v \leq 0.3\,\mathrm{s\,km^{-1}}$.
7. *Black pluses* represent Δv as obtained from successful fits of a Gaussian cutoff that were manually excluded from fitting (3.43) for being clear outliers.

5.2 Redshift $z = 4.0$

The density and temperature dependencies of Δv are shown in figures (5.1a) and (5.1b), respectively. For the vast majority of densities and thermal scales considered here, peculiar velocities produced a Gaussian cutoff, with the exception of the two lowest densities with $\langle n_H \rangle \leq 8.105\,\mathrm{m^{-3}}$, i.e. (4.1) evaluated with $z_{\mathrm{LOS}} = 2.0$ or $z_{\mathrm{LOS}} = 2.5$; these were rejected for being based on too few data points, suggesting that a cutoff is no longer noticeably present. This can be explained if the density has become so low that the Ly-α forest is no longer dominated absorption, since absorption features are not broadened by peculiar velocities.
Furthermore, the cutoff scales at the two highest densities considered here, $\langle n_H \rangle \geq 89.711\,\mathrm{m^{-3}}$, were excluded from the data to which (3.43) was fitted. At the highest density the flux had become too low to produce a reliable cutoff, but at $\langle n_H \rangle = 89.711\,\mathrm{m^{-3}}$ the peculiar velocities produced a Gaussian cutoff that could in principle be fitted reliably. We excluded it because it clearly deviates from the trend in most lower-density data points; this deviation may be taken as a clue that (3.43) fails at high densities.
Generally however, Δv could be fitted rather well by (3.43). This was confirmed by the χ^2_{red}-values of this model, which were 0.47 ± 0.37 and 0.37 ± 0.35 for the density and temperature dependence respectively. The values of A and B as fitted from the density and temperature dependency individually differed 1.7σ and 0.7σ respectively.
The dependence of Δv on σ_u is shown in figure 5.2a. A Gaussian cutoff was successfully fitted at most σ_u, except for two high σ_u ($90\,\mathrm{km\,s^{-1}}$ and $100\,\mathrm{km\,s^{-1}}$); at these high σ_u, the Gaussian fit did not pass the χ^2-test. We can also note that a directly proportional fit is a relatively poor description of the dependency of Δv on σ_u; indeed, such a fit has $\chi^2_{\mathrm{red}} = 1.88 \pm 0.34$ and we can reject it. Interestingly however, C as determined from the weighted average of $\frac{\Delta v}{\sigma_u}$ is $C = 0.638 \pm 0.014$, while the C as predicted from the final A and B through (4.10) is 0.644 ± 0.027, differing a mere 0.2σ.
Finally, figure 5.2b shows that Δv did not significantly change with the T_0 that is used for thermal broadening; the weighted average has $\chi^2_{\mathrm{red}} = 0.37 \pm 0.39$.

Version of July 8, 2022– Created July 8, 2022 - 21:51

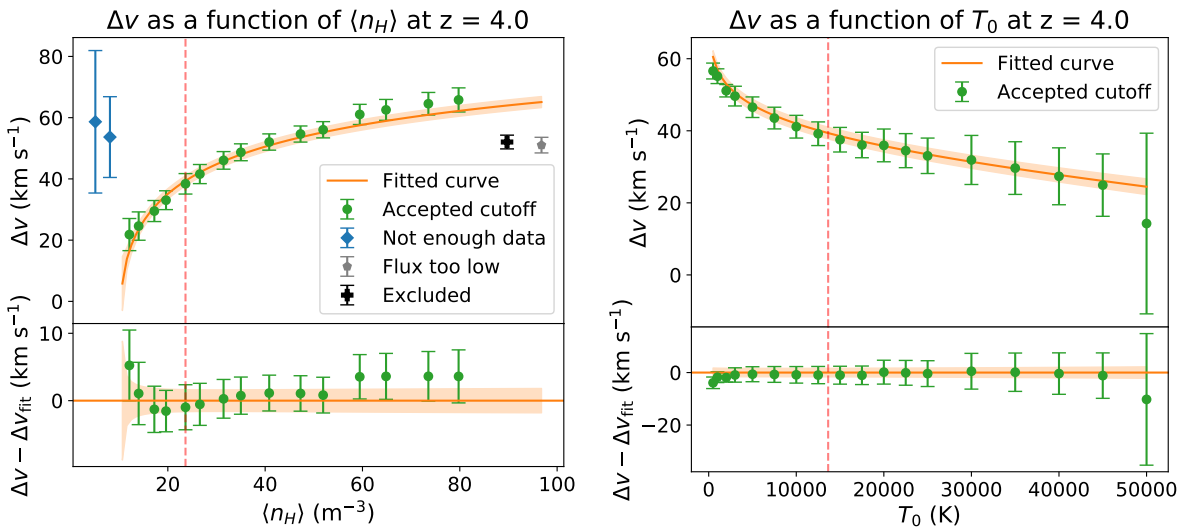

(a) *(b)*

Figure 5.1: *Figure 5.1a shows how Δv depends on $\langle n_H \rangle$ at $z = 4.0$, figure 5.1b shows how Δv depends on T_0 at this redshift. The meaning of the symbols is as described in section 5.1; the solid orange curve represents the final fit of (3.43) to the data (i.e. after averaging A and B), with the error margin marked as a shaded orange region. The lower panels show the difference between the realised and modelled cutoff scale. The vertical dashed red lines mark the realistic $\langle n_H \rangle$ and T_0 at $z = 4.0$.*

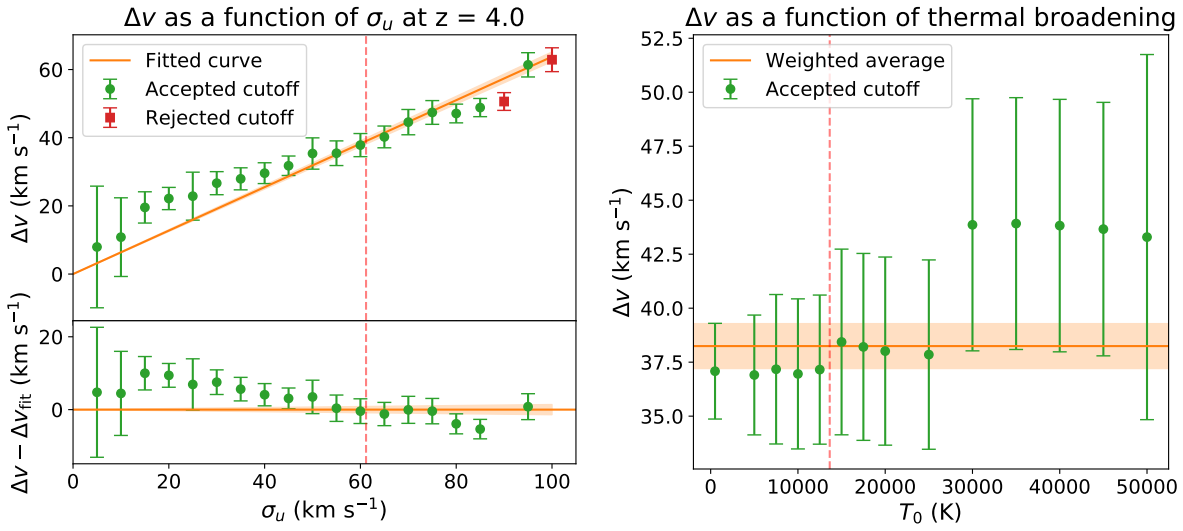

(a) *(b)*

Figure 5.2: *Figure 5.2a shows how Δv depends on the peculiar velocity dispersion σ_u at $z = 4.0$, while figure 5.2b shows the dependence of Δv at $z = 4.0$ on thermal broadening, which is parameterised by the T_0 used to calculate the thermal broadening. The meaning of symbols is as described in section 5.1, and the orange curve shows the best fit of the respective models (i.e. proportional dependence in figure 5.2a and no dependence in figure 5.2b), with the error margins on the modelled cutoff scale presented as a shaded orange region. In figure 5.2a, the lower frame shows the difference between the realised and modelled cutoff scale.*

5.3 Redshift $z = 4.5$

At $z = 4.5$, we should note that in principle the method as described in chapter 4 yields values of A and B that do not allow (3.43) to satisfactorily fit the realised cutoff scales, as they yield $\chi^2_{\text{red}} = 2.08 \pm 0.38$ and $\chi^2_{\text{red}} = 2.48 \pm 0.35$ for the density and temperature dependencies respectively. This is however mostly due to the fact that the A and B that were fitted to the temperature dependence perform relatively poor; indeed, using (3.43) as fitted to the density dependence yields an acceptable fit to the temperature dependence as well. This also does not increase the error margins on A and B by much, as they were already dominated by the fit to the density dependence (the error on A increases by some 0.0016 or 16.3%, and the error on B increases by 0.0010 or 0.12% with respect to the weighted average values). Because of this, we proceed with the A and B as fitted to the density dependence.
The dependence of Δv on $\langle n_H \rangle$ and T_0 is shown in figures 5.3a and 5.3b, respectively. Again, the vast majority of densities and temperatures allowed for a Gaussian cutoff to be fitted acceptably well, except for the two lowest densities ($\langle n_H \rangle \leq 8.105\,\text{m}^{-3}$) for which there was no noticeable cutoff at all. Furthermore, the Δv at the two highest densities ($\langle n_H \rangle \geq 89.711\,\text{m}^{-3}$) were excluded because the underlying Ly-α forests had $\langle F \rangle < 0.005$; the cutoff scales fitted to the resulting $\mathcal{D}$ were, however, consistent with the prediction of (3.43) based on the other Δv. Also note in figure 5.3b that almost all realised Δv were above the final modelled Δv, suggesting that a higher value of A might be more applicable to the temperature dependence; the A as fitted by the density dependence differs some 2.5σ from the A fitted by the temperature dependence (for B, this difference is only 1.0σ due to the large error on the value from the temperature dependence). Nevertheless, the χ^2_{red} of the fit of (3.43) to the density dependence are 1.14 ± 0.38 and 1.26 ± 0.35 for the density and temperature dependencies respectively and thus we cannot reject (3.43) as fitted to the density dependence of Δv as a description of the temperature dependence of Δv.
As figure 5.4a shows, (4.5) was a good model for $\mathcal{D}$ for all σ_u considered here. However, the direct proportionality of (3.43) remained a poor description of the dependence of Δv on σ_u ($\chi^2_{\text{red}} = 10.16 \pm 0.32$), with Δv larger than the directly proportional model at low σ_u and smaller at high σ_u. Again, it is intriguing that the average slope in figure 5.4a is $C = 0.7203 \pm 0.0088$, whereas (4.10) with A and B as fitted to the density and temperature dependencies predict $C = 0.740 \pm 0.043$, a difference of 0.4σ.
Finally, figure 5.4b, which shows Δv as a function of the T_0 used for thermal broadening, demonstrates that Δv does not appear to depend on thermal broadening; the weighted average has $\chi^2_{\text{red}} = 1.32 \pm 0.45$, meaning that we cannot reject independence of Δv from thermal broadening.

Version of July 8, 2022– Created July 8, 2022 - 21:51

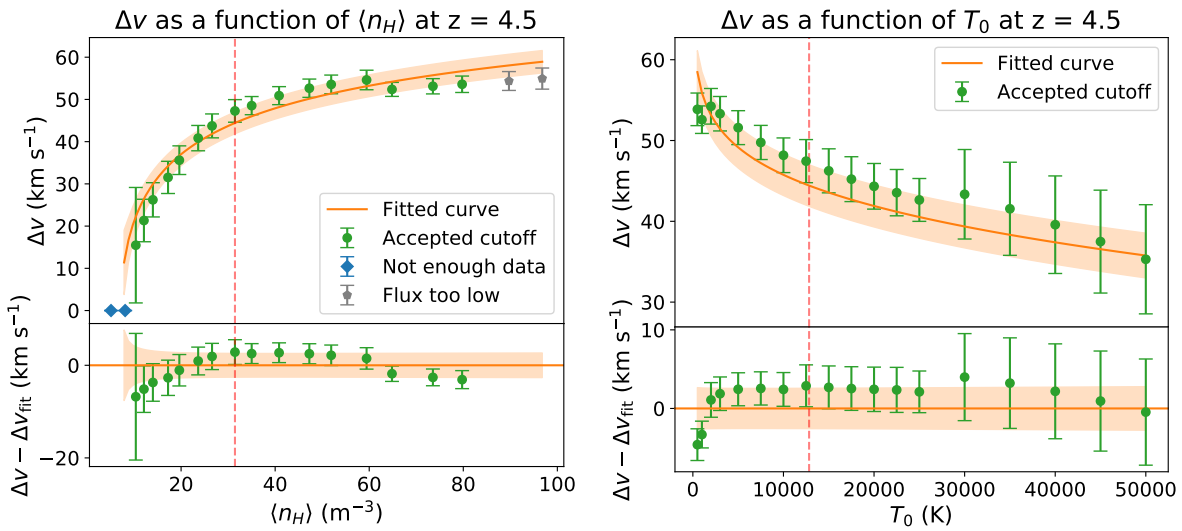

(a) ***(b)***

Figure 5.3: *The same as figure 5.1, now evaluated at $z = 4.5$ and with the orange curve representing (3.43) as fitted to the density dependence. Note that in figure 5.3b, most realised Δv are above the modelled value but follow the same general curve, suggesting that a higher value of A might be more applicable.*

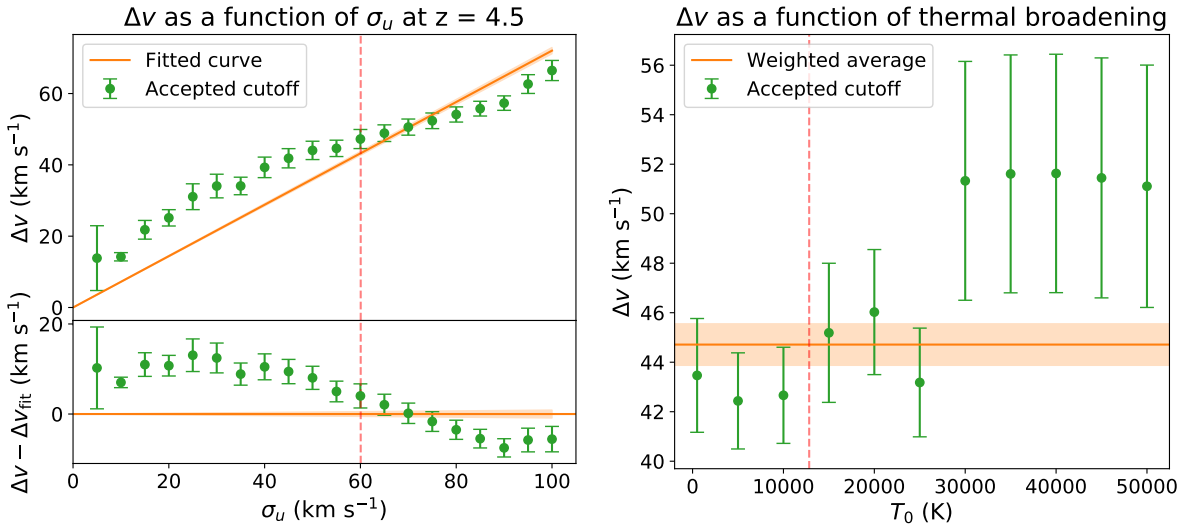

(a) ***(b)***

Figure 5.4: *The same as figure 5.2, now evaluated at $z = 4.5$. Although there are Δv for which the weighted average falls outside their error margin, we still cannot exclude that Δv is independent of thermal broadening.*

Version of July 8, 2022– Created July 8, 2022 - 21:51

5.4 Redshift $z = 5.0$

The density and temperature dependencies of Δv at $z = 5.0$ are shown in figures 5.5a and 5.5b respectively. At nearly all $\langle n_H \rangle$ considered here the peculiar velocities produced a Gaussian cutoff; the exceptions were the two lowest densities $\langle n_H \rangle \leq 8.105\,\mathrm{m}^{-3}$, where the cutoff scale was smaller than $2.09\,\mathrm{km\,s}^{-1}$ and thus not considered to be detectable for $k_v \leq 0.3\,\mathrm{s\,km}^{-1}$. Also, the Δv at the two highest densities $\langle n_H \rangle \geq 79.753\,\mathrm{m}^{-3}$ were excluded from the fitting procedure of (3.43) for being based on Ly-α forests with $\langle F \rangle < 0.005$. The same happened to the Δv at the two lowest T_0 ($T_0 = 500\,\mathrm{K}$ and $1000\,\mathrm{K}$). Besides these, the cutoff scales at $z = 5.0$ agreed to a high degree with the dependencies predicted from (3.43), with the final fits (i.e. after averaging A and B) yielding $\chi^2_{\mathrm{red}} = 0.14 \pm 0.41$ and $\chi^2_{\mathrm{red}} = 0.19 \pm 0.38$; the A and B fitted to the density and temperature dependencies differ 0.9σ and 0.8σ respectively. Hence, (3.43) provides an excellent description of Δv as a function of $\langle n_H \rangle$ and T_0 at $z = 5.0$.
Regarding the dependence of Δv on σ_u, which is shown in figure 5.6a, we may remark that it is qualitatively similar to the one at $z = 4.5$: the realised Δv were higher than the proportional model at low σ_u and lower at high σ_u, with the directly proportional fit rejected because $\chi^2_{\mathrm{red}} = 8.06 \pm 0.32$. The average slope in figure 5.6a was $C = 0.7408 \pm 0.0086$; the one predicted from the fitted A and B through (4.10) was $C = 0.793 \pm 0.032$, thus differing of 1.6σ.
The independence of Δv from thermal broadening is less apparent from figure 5.6b, which shows Δv as a function of the T_0 used for thermal broadening, than it was from equivalent figures (i.e. figures 5.2b and 5.4b) at lower redshift; still, a Δv that is independent of thermal broadening has $\chi^2_{\mathrm{red}} = 1.69 \pm 0.45$, so we cannot reject it.

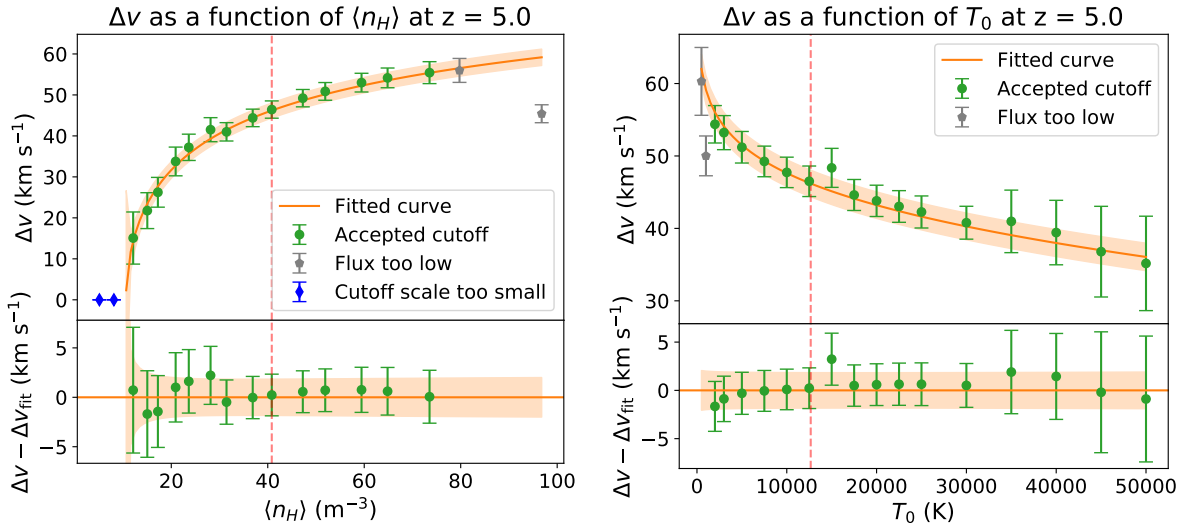

(a) ***(b)***

Figure 5.5: *The same as figure 5.1, now evaluated at $z = 5.0$.*

Version of July 8, 2022– Created July 8, 2022 - 21:51

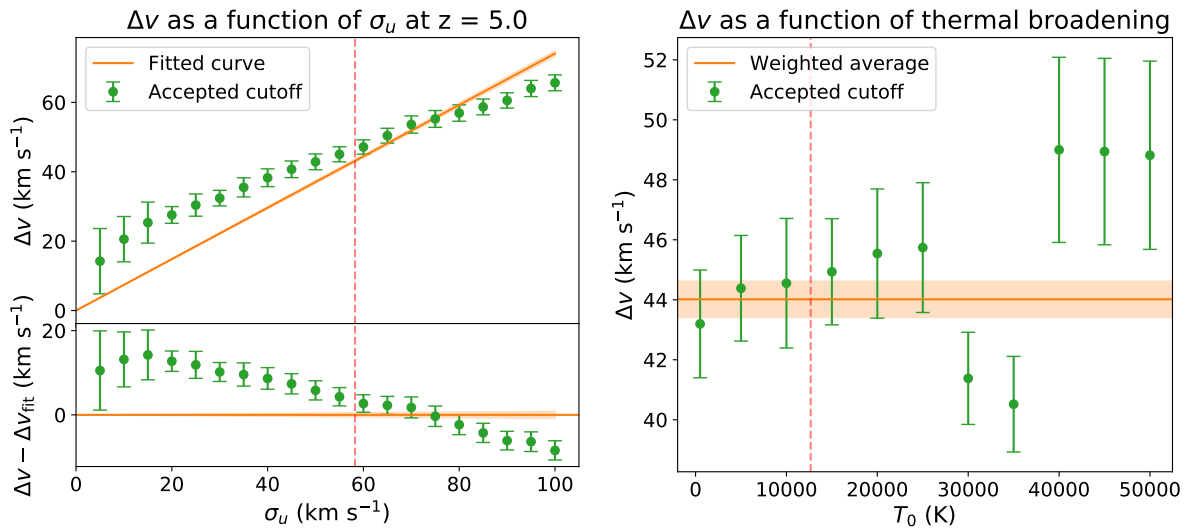

(a) *(b)*

Figure 5.6: *The same as figure 5.2, now evaluated at $z = 5.0$.*

5.5 Redshift $z = 5.5$

In figure 5.7a, the dependence of Δv on $\langle n_H \rangle$ at $z = 5.5$ is shown. The only densities that did not allow for a convincing Gaussian cutoff due to peculiar velocities are the two lowest $\langle n_H \rangle \leq 8.105\,\mathrm{m}^{-3}$, either because the fitted cutoff scale was smaller than $2.09\,\mathrm{km\ s}^{-1}$ or because the Gaussian fit was based on too few data points. Otherwise, the dependency of Δv on $\langle n_H \rangle$ is described relatively well by (3.43).
Figure 5.7b shows how Δv changes with T_0. At very low temperatures $T_0 \leq 3000\,\mathrm{K}$, the neutral hydrogen density is so high (because $n_{\mathrm{HI}} \propto \alpha_{\mathrm{HII}}$ and approximately $\alpha_{\mathrm{HII}} \propto T^{-0.7}$) that the Ly-$\alpha$ forest has $\langle F \rangle < 0.005$, leading to a rejection of the cutoff induced by peculiar velocities. Subsequently, there is a break in the trend as Δv suddenly increases at $T_0 = 30 \times 10^3\,\mathrm{K}$ and then starts to decrease with increasing T_0 again. Because of this break in the general trend, we decided to exclude all Δv at $T_0 \geq 30\,000\,\mathrm{K}$ when fitting (3.43) to Δv as a function of T_0. This decision was further justified because A and B, when fitted to the density dependence of Δv, provided a satisfactory description of Δv at low temperatures, while the high-temperature realised values of Δv were systematically higher than predicted based on the fit of (3.43) to the density dependence of Δv.
To further justify this exclusion, we considered qualitative differences between $\mathcal{D}$ at $T_0 < 30\,000\,\mathrm{K}$ and $T_0 \geq 30\,000\,\mathrm{K}$. As an example, figure 5.8 compares $\mathcal{D}$ at $T_0 = 25 \times 10^3\,\mathrm{K}$ and at $T_0 = 40 \times 10^3\,\mathrm{K}$. From this figure, it is clear that raising the temperature modified $\mathcal{D}$, but instead of cutting off at a larger scale as the least-squares fit indicated, $\mathcal{D}$ should cut off at smaller scales for $T_0 = 40 \times 10^3\,\mathrm{K}$ than for $T_0 = 25 \times 10^3\,\mathrm{K}$. The reason that the fitted cutoff at the former temperature occurred at a larger scale than at the latter is, based on figure 5.8b which is representative for all $T_0 \geq 30 \times 10^3\,\mathrm{K}$, that the recovery effect caused the minimum in $\mathcal{D}$ to be less well defined at high temperatures. As a result, the k_v at which $\mathcal{D}$ was minimised can experience a sudden decrease with rising temperature as one mainly noise-dominated minimum is raised above another one with increasing T_0. In figure 5.8, this is actually visible: in figure

Version of July 8, 2022– Created July 8, 2022 - 21:51

5.8a, the minimum occurs at a k_v well above $\frac{2\pi}{\sigma_u}$, while in figure 5.8b the minimum occurs at a k_v below $\frac{2\pi}{\sigma_u}$. This sudden decrease in range of k_v to which (4.5) is fitted caused the fit to err on the side of a large Δv. As the temperature increases further, the k_v at which the minimum occurs does not make another such jump and thus Δv evolves according to (3.43) again, explaining why the excluded Δv appear on a similar but translated curve in figure 5.7b.

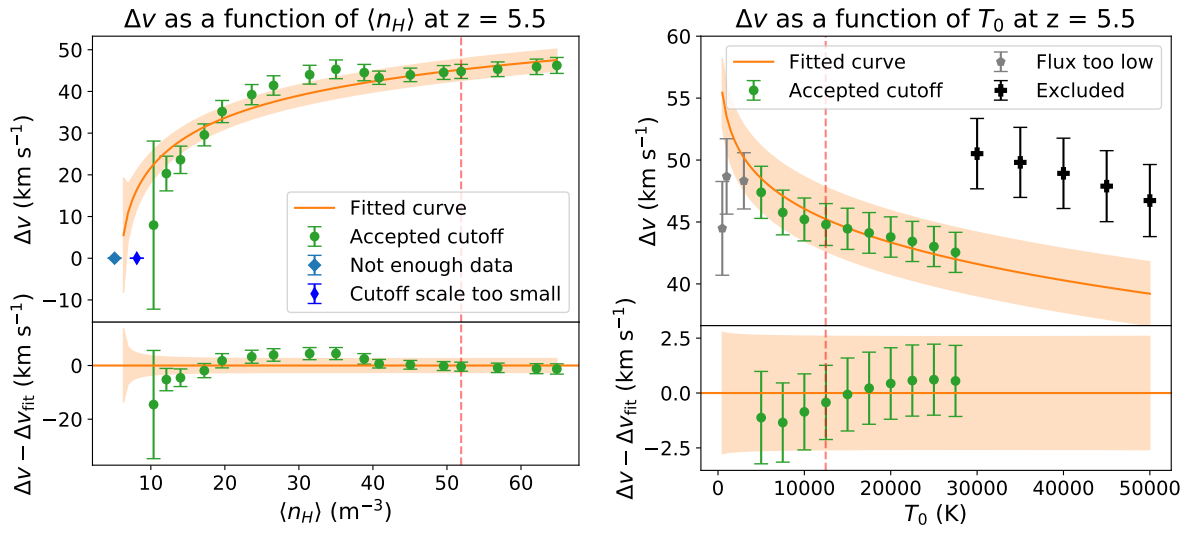

(a) ***(b)***

Figure 5.7: *The same as figure 5.1, now evaluated at* $z = 5.5$.

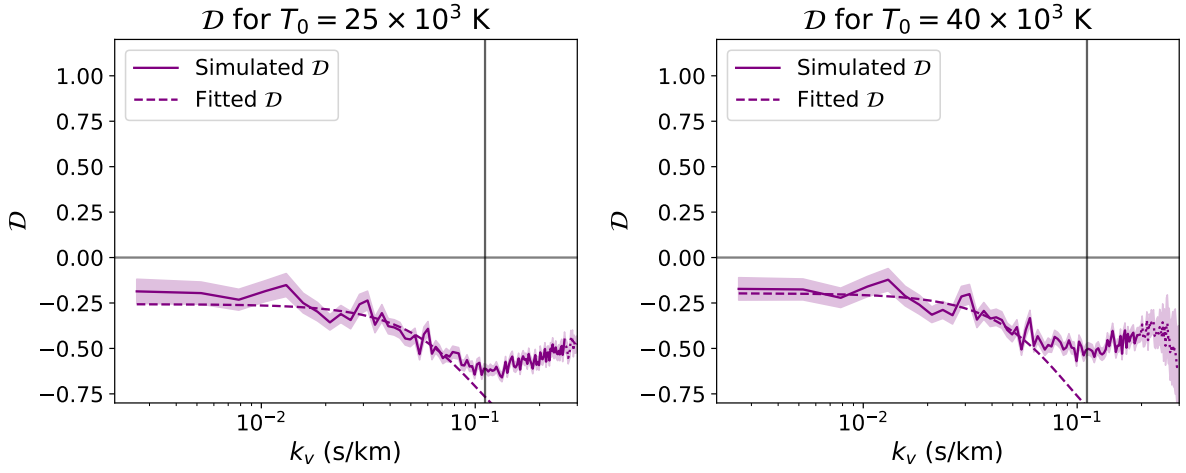

(a) ***(b)***

Figure 5.8: *Figure 5.8a shows* $\mathcal{D}$ *(the solid curve) as a function of* k_v *at* $z = 5.5$ *with thermal scale* $T_0 = 25 \times 10^3$ K*, while figure 5.8b shows* $\mathcal{D}$ *at the same redshift but with* $T_0 = 40 \times 10^3$ K*. The dashed curves are the best fitting Gaussian cutoffs at low* k_v*, the solid vertical line marks the scale* $k_v = 2\pi/\sigma_u$ *and the dotted part of the curve representing* $\mathcal{D}$ *marks scales for which either or both* Δ_F^2 *with and without peculiar velocities is less than* 10^{-3}.

After excluding the cutoff scales at $T_0 \geq 30 \times 10^3$ K, the weighted averages of A and B were completely dominated by the values fitted to the density dependence of Δv,

Version of July 8, 2022– Created July 8, 2022 - 21:51

which we consider to be reasonable as it is based on much more data points than were accepted for the temperature dependence of Δv. The density and temperature dependencies of Δv had $\chi^2_{\text{red}} = 1.36 \pm 0.37$ and 0.20 ± 0.50 respectively.
Finally, figures 5.9 and 5.9b show how Δv depended on σ_u and thermal broadening. Again, the behaviour of Δv as a function of σ_u couldn't be described adequately through a direct proportionality ($\chi^2_{\text{red}} = 6.63 \pm 0.34$); instead, Δv was larger than such a proportionality would predict at small σ_u and smaller at large σ_u. The average slope $C = 0.7860 \pm 0.0080$ differed a mere 0.3σ from the value as calculated from A and B, which was 0.800 ± 0.046. As figure 5.9b demonstrates, Δv did not depend significantly on the T_0 used for thermal broadening ($\chi^2_{\text{red}} = 1.13 \pm 0.45$).

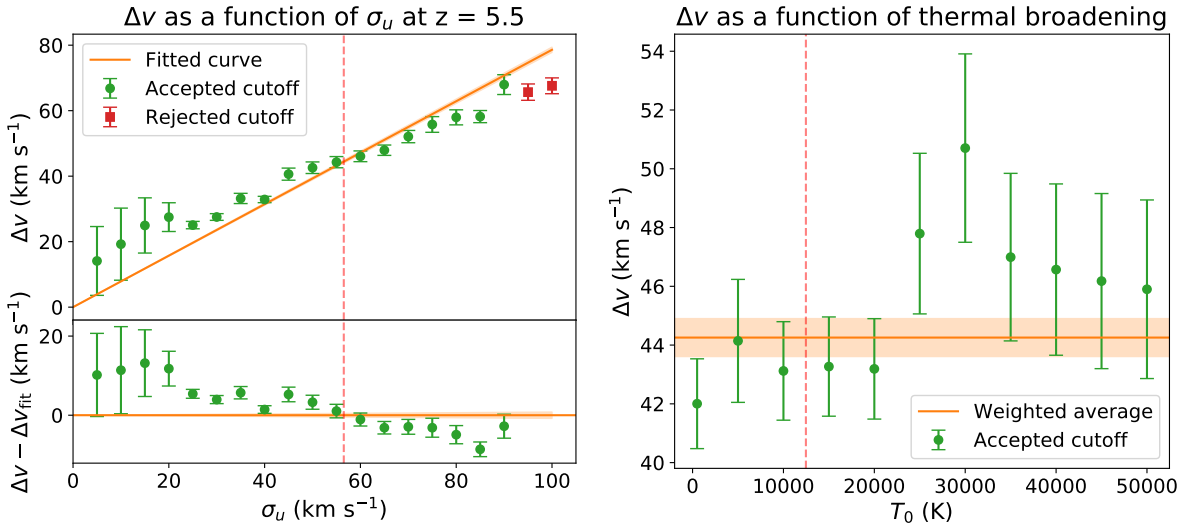

(a) *(b)*

Figure 5.9: *The same as figure 5.2, now evaluated at $z = 5.5$.*

5.6 Redshift $z = 6.0$

Figure 5.10a shows the dependence of Δv on the density at $z = 6.0$, and a Gaussian cutoff is a reasonable description of the influence of peculiar velocities on the FPS for a considerable range of densities. At the lowest densities $\langle n_H \rangle \leq 8.105\,\text{m}^{-3}$, a Gaussian cutoff (4.5) was rejected because it was either a poor description of $\mathcal{D}$ (did not pass the χ^2-test) or because such a cutoff was absent. At high densities $\langle n_H \rangle \geq 64.842\,\text{m}^{-3}$, the cutoff was excluded from the data used for fitting because $\langle F \rangle$ in the Ly-α forest was too low. Note that this happened at lower densities than at lower redshifts; this can be understood through (2.48), which states that density perturbations grow proportionally to the scale factor. Hence, at large redshifts we expect the density field to be more homogeneous than at low redshifts; this means that voids are closer to the cosmic average density, and thus that a modest density already causes voids to be dense enough to nearly completely block Ly-α transmission.
Figure 5.10b shows the dependence of Δv on T_0. As can be seen, temperatures $T_0 \leq 12.5 \times 10^3$ K yielded Ly-α forests with $\langle F \rangle < 0.005$. This happened for higher temperatures than at lower redshifts, which can be understood by recalling that approximately, $\alpha_{\text{HII}} \propto T^{-0.7}$; through (3.6), a low temperature thus leads to a high neutral hydrogen

Version of July 8, 2022– Created July 8, 2022 - 21:51

density. Similarly to our earlier argument, even a modest neutral hydrogen density will allow voids to nearly completely absorb Ly-α radiation at these high redshifts, because the density field is more homogeneous than at low redshift.
For $T_0 > 12.5 \times 10^3$ K, Δv varied far more erratically; because of this erratic behaviour, A and B as fitted to the density and temperature dependence could not be reconciled (they differed 4.6σ and 1.7σ respectively). Indeed, fitting (3.43) to the density and temperature dependencies individually yielded $\chi^2_{\text{red}} = 3.48 \pm 0.50$ and $\chi^2_{\text{red}} = 3.14 \pm 0.43$ respectively, indicating that (3.43) can no longer accurately describe the dependencies of Δv at $z = 6.0$. To give an idea of the severity of this failure, figure 5.10 shows the best fit of (3.43) to the density and temperature dependence of Δv individually.
When calculating Δv as a function of σ_u, it was noted that for all σ_u considered here, the FPS was based on Ly-α forests with $\langle F \rangle < 0.005$. However, as evidenced by Δv at high densities in figure 5.3a, a Δv based on Ly-α forests with $\langle F \rangle$ slightly below the (essentially arbitrary) flux limit imposed here can sometimes still be adequately described within the framework of (3.43). Since the $\langle F \rangle$ of the Ly-α forests upon which Δv is based is only slightly below 0.005 for the simulated T_0 and $\langle n_H \rangle$ (it is roughly 0.0037), it was decided to temporarily suspend the requirement on $\langle F \rangle$ so that the dependence of Δv on σ_u could be analysed. As can be seen from figure 5.11a, there was again no direct proportionality ($\chi^2_{\text{red}} = 6.64 \pm 0.32$). Furthermore, the average slope of $C = 0.7264 \pm 0.0087$ differs some 1.7σ from the slope predicted from the density dependence (0.854 ± 0.073) and 2.4σ from the slope predicted from the temperature dependence (0.97 ± 0.10); these relatively large discrepancies (when compared to the agreement at lower redshift) should not come as a surprise, as the fits to the density and temperature dependence were rejected.
Finally, figure 5.11b shows how Δv varied with the T_0 used for thermal broadening. The data as shown has $\chi^2_{\text{red}} = 1.62 \pm 0.45$ and thus cannot be rejected as being independent of thermal broadening.

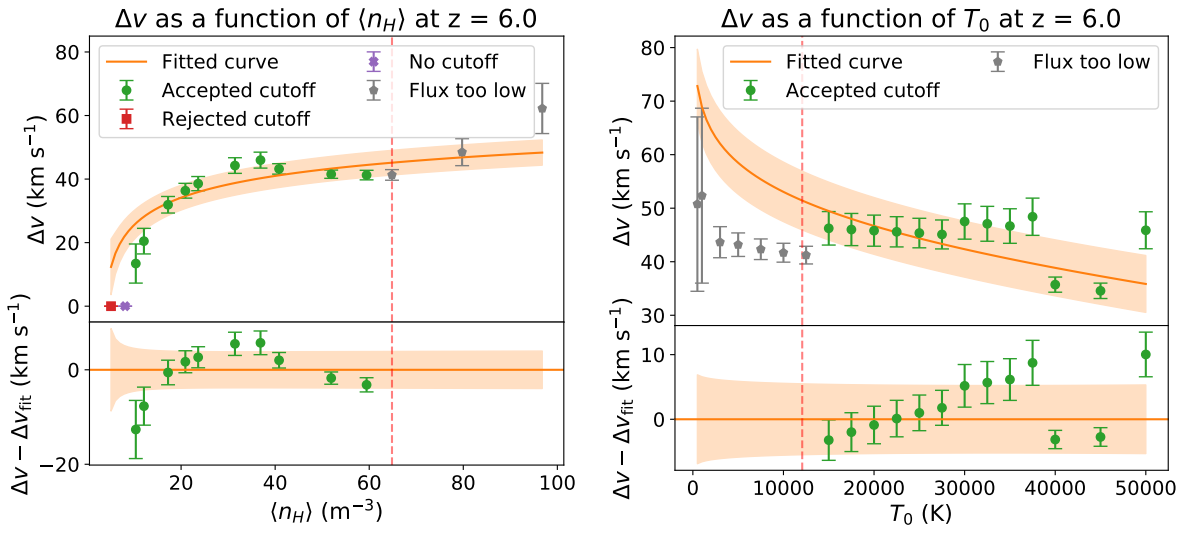

(a) ***(b)***

Figure 5.10: *The same as figure 5.1, now evaluated at $z = 6.0$. Note that the orange curves shown here represent (3.43), fitted to the respective dependencies of Δv; this was done because (3.43) does not describe Δv accurately in either case.*

Version of July 8, 2022– Created July 8, 2022 - 21:51

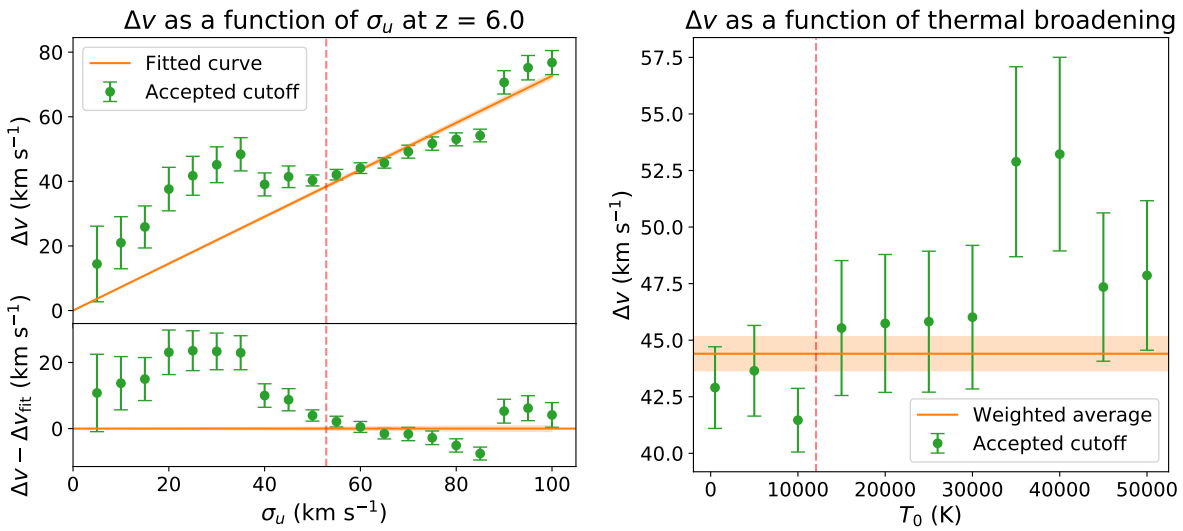

(a) *(b)*

Figure 5.11: *The same as figure 5.2, now evaluated at $z = 6.0$. Note that to produce figure 5.11a, the rejection based on a low $\langle F \rangle$ was temporarily suspended; had this not been done, all fits in figure 5.11a would have been rejected for being based on Ly-α forests with $\langle F \rangle \leq 0.005$.*

5.7 The redshift dependence of A and B

The preceding has established that (4.5) is typically a good model for $\mathcal{D}$ at low k_v and that furthermore (3.43) is a reasonable description of the dependence of Δv on $\langle n_H \rangle$, T_0, and, on average, σ_u, for $z \leq 5.5$. We may now consider the redshift dependence of A and B. This dependence is shown in figures 5.12a and 5.12b respectively. The simplest assumption we might make for the redshift dependence of A and B is that there is none; to test this assumption, we may subject the weighted averages of A and B across different redshifts to the χ^2-test. For A, the analogue of (4.9) yielded $\chi^2_{\text{red}} = 12.44 \pm 0.82$, while for B it yielded $\chi^2_{\text{red}} = 2.53 \pm 0.82$. Although we cannot justify the assumption $n \gg 1$ that lead to the error margin on χ^2_{red} anymore (since $n = 3$), the χ^2_{red} for A was so far away from 1 that we concluded that it is redshift dependent. For B, the situation is less clear-cut as it had χ^2_{red} relatively close to 1, hence we cannot reject the notion of a constant B based on the data presented here.

Version of July 8, 2022– Created July 8, 2022 - 21:51

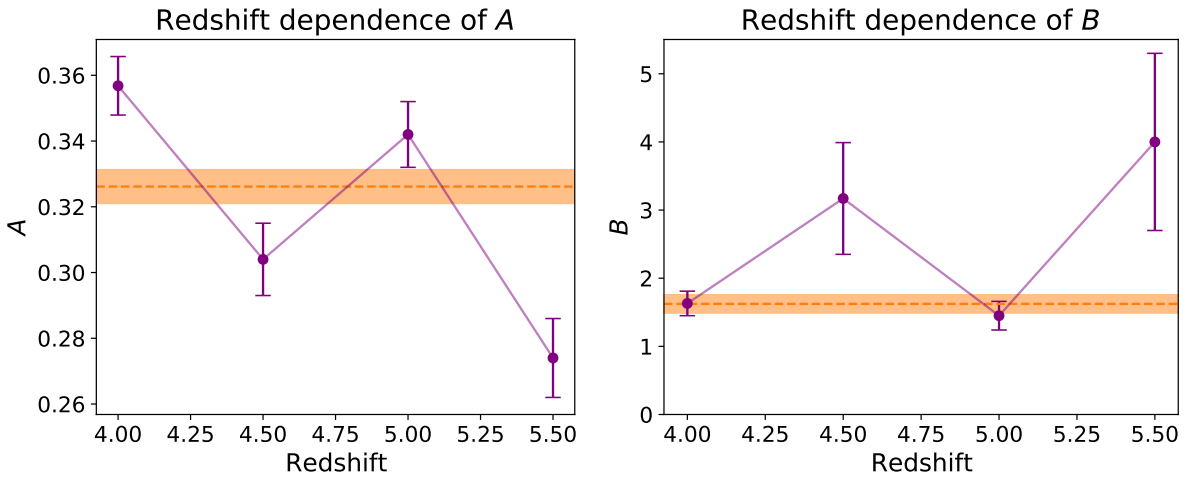

(a) *(b)*

Figure 5.12: *The redshift dependence of the A (figure 5.12a) and B (figure 5.12b) parameters from (3.43) for $z \leq 5.5$. The fitted parameters are shown as purple circles connected by solid lines; their average, weighted by the inverse variance, is shown as a horizontal dashed orange line, with its error margin shown as a shaded orange region. Note that A and B at $z = 4.5$ were based on the fit of (3.43) to the density dependence of Δv only. Also note the significantly different vertical axes.*

5.8 The redshift dependence of Δv

Finally, we considered how Δv changed with redshift under the simulated conditions, and how this compared to the characteristic scales on which thermal broadening and pressure broadening influence the FPS (assuming a temperature T_0). The result of this comparison can be seen in figure 5.13, which shows Δv at various redshifts for the simulated conditions together with b_T as defined in (3.21) and the spatial scale $v_F = \frac{2\pi}{k_F} H(z_{\text{LOS}})$ corresponding to the filtering scale k_F as defined in (2.45) and thus a characteristic scale of pressure broadening. The only Gaussian fit to $\mathcal{D}$ that could possibly be unrealistic was the fit at $z = 6.0$, as $\langle F \rangle < 0.005$ at this redshift.
In general, the peculiar velocities induce a cutoff in the FPS at a significantly larger scale than thermal broadening or pressure broadening (which is parametrised by k_F), indicating that the total cutoff in the FPS should be dominated by Δv instead of b_T or v_F. However, as figure 5.14 shows, the FPS mostly retains the general shape of the FPS without peculiar velocities. The reason for this apparent discrepancy is the recovery effect, which nullifies the impact of peculiar velocities at high k_v.

Version of July 8, 2022– Created July 8, 2022 - 21:51

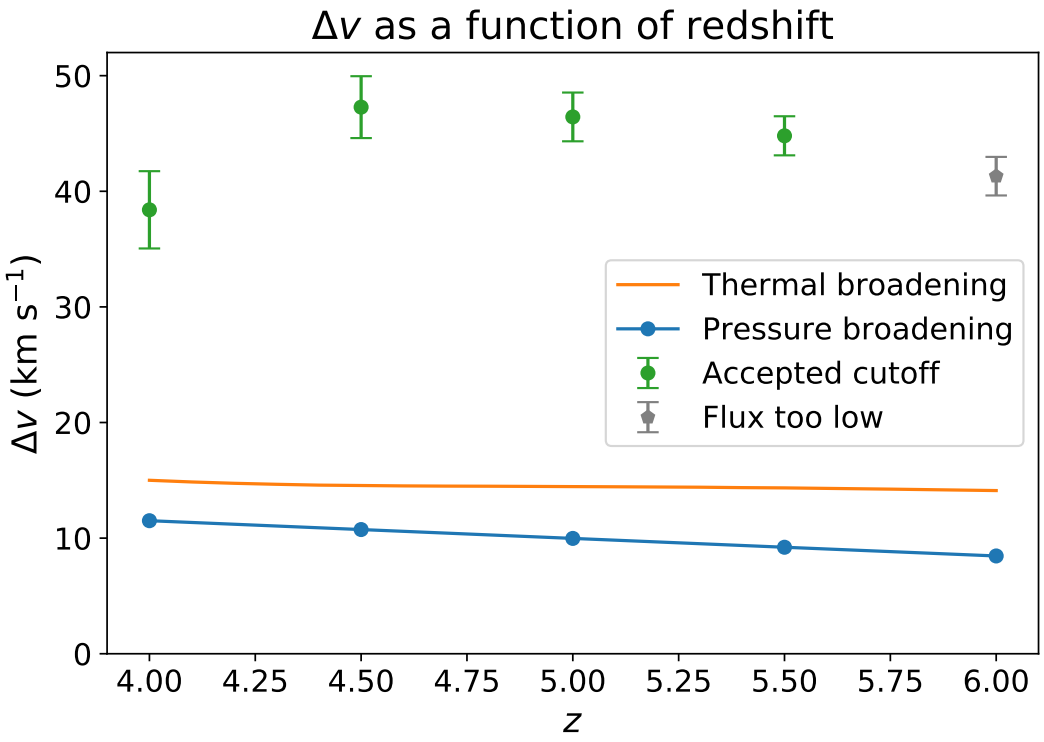

Figure 5.13: *The realistic redshift evolution of several cutoff scales. In the symbols of section 5.1, the cutoff scale due to peculiar velocities is shown; the solid orange curve shows the thermal broadening scale (3.21) at $T = T_0$; and finally the light blue line with filled circles shows the filtering scale $H(z_{\mathrm{LOS}}) \cdot 2\pi/k_F$, as calculated from (2.45) with the simulated thermal history and the assumption that the IGM is an ideal gas with $T = 0$ for $z > 12.0$ and $T = T_0$ otherwise.*

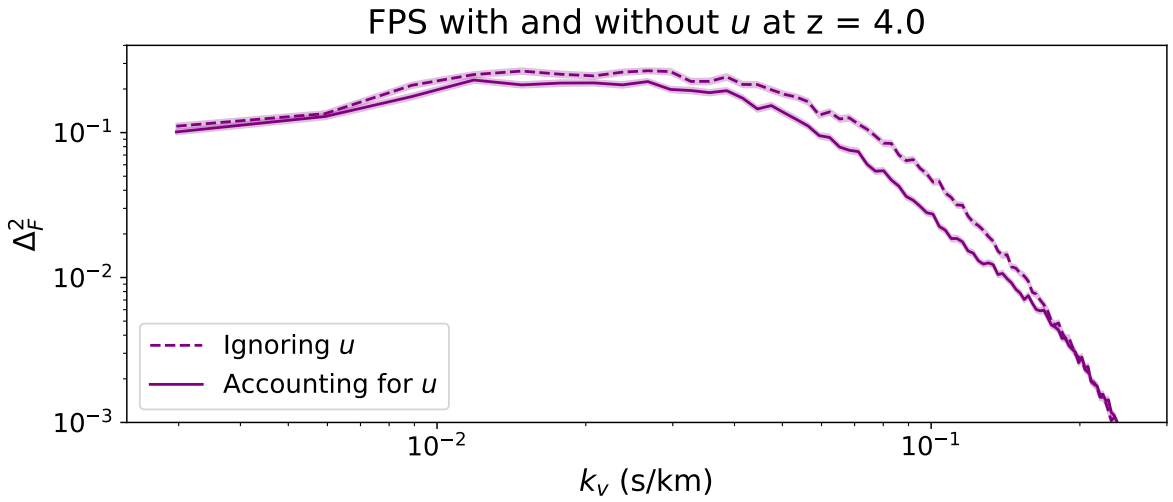

Figure 5.14: *The FPS with and without peculiar velocities at $z = 4.0$, calculated with the simulated thermal parameters and density. The solid curve represents the FPS calculated while taking peculiar velocities into account, while the dashed curve shows the FPS calculated without peculiar velocities. Shaded regions indicate the error margins.*

Version of July 8, 2022– Created July 8, 2022 - 21:51

Chapter 6

Discussion

This thesis set out with the goal of quantifying the impact of peculiar velocities on the flux power spectrum (FPS) of the Ly-α forest. The eventual application of this is to use the Ly-α forest to learn about the large-scale structure (LSS) of the universe, and hence we first introduced a treatment of the description and evolution of the LSS in its linear stages in chapter 2. Subsequently, in chapter 3, we introduced an important baryonic component of the LSS, the intergalactic medium (IGM), considering its ionisation state and its optical depth to Ly-α radiation. Chapter 3 ended with the central proposal of this thesis, namely equation (3.43), which defines a characteristic scale Δv on which peculiar velocities impact the FPS. It proposes a direct proportionality of Δv to the dispersion in the peculiar velocities, and a dependence on the square root of the logarithm of, among others, the average hydrogen density and the recombination rate, while also implying independence of Δv from thermal broadening.
Chapter 4 then introduced the methods employed to test this model. It very briefly described the simulations used in this thesis and how the FPS was extracted from them. After this, it proposed an analogy between the pressure broadening of baryonic structures relative to the underlying dark matter distribution and the broadening of transmission features in the Ly-α forest due to peculiar velocities, which tend to concentrate the optical depth in high peaks. Based on this analogy, it proposed that peculiar velocities could introduce a Gaussian cutoff at spatial scale Δv to the FPS of an absorption-dominated Ly-α forest. This cutoff should then be visible in the relative deviation $\mathcal{D}$ between the FPS calculated with and without peculiar velocities. However, it immediately became clear that a Gaussian cutoff was not an appropriate description of $\mathcal{D}$ over the entire range of k_v considered here, owing to an effect we dubbed the recovery effect. We worked around this effect by limiting the range of k_v to which we fitted (4.5), to exclude scales on which the recovery effect dominates.
Equipped with the methods from chapter 4, we then proceeded in chapter 5 to present their results. We found that the Gaussian cutoff model yields acceptable results for a wide range of densities, temperature scales, peculiar velocity dispersions and amounts of thermal broadening at nearly all redshifts considered here. It was even demonstrated that at least for redshifts $4.0 \leq z \leq 5.5$, (3.43) provided an acceptable description of the dependence of Δv on the mean hydrogen density and T_0, and independence of Δv from the amount of thermal broadening could not be excluded. Although the dependence of Δv on σ_u was more complex than predicted by (3.43), it still correctly

Version of July 8, 2022– Created July 8, 2022 - 21:51

predicted the average ratio between Δv and σ_u.
Even so, the dependencies of Δv at $z = 6.0$ proved to be more complex and (3.43) had to be rejected as a model for Δv; indeed, even the Gaussian cutoff (4.5) did not apply as consistently as it did at lower redshift. We explained this as being due to the higher degree of homogeneity at such a high redshift. Hence, a small neutral hydrogen density could render even relative voids nearly opaque to Ly-α radiation as they are already much closer to the cosmic average density. The only prediction of (3.43) that could not be rejected at $z = 6.0$ was the independence of Δv from thermal broadening.

6.1 The recovery effect

As mentioned before, (3.43) has been rejected as a description of Δv at $z = 6.0$. Another instance in which (3.43) appeared to fail as a description of Δv was in the temperature dependence of Δv at $z = 5.5$, where temperatures above 30×10^3 K were manually excluded to reach agreement between the density and temperature dependencies of Δv, and in general to allow the latter to be described by (3.43) at all. This exclusion was justified as an increased temperature lead to a stronger recovery effect, which in turn artificially caused a sudden decrease in the range of k_v used for fitting (4.5). Indeed, it may be a general fact that the method employed here to select a range of k_v to use for fitting (4.5) suffers from such numerical artefacts. For example, the sudden changes in Δv as a function of T_0 used for thermal broadening seen at high temperatures at all redshifts (i.e. in figures 5.2b, 5.4b, 5.6b, 5.9b and 5.11b) all appear associated with a change of typically 3 to 6 on a total of $\sim 20 - 30$ in the number of points used to fit (4.5); a decrease in the number of points appeared to be associated with a higher Δv while an increase seemed associated with a lower Δv. The erratic behaviour of Δv at $z = 6.0$ may possibly be explained similarly.
To optimise the selection procedure, it would be very advantageous to have a description of the recovery effect; if not at all scales, then at least on the scales probed here. In this thesis we mainly attempted to properly ignore the recovery effect, but future research might attempt to provide such a more complete description.
However, we may still consider the origin of this effect. A similar effect was already described at the beginning of section 3.4, which motivated that peculiar velocities should make absorption features more narrow and thus would add power to the FPS, especially at small scales. This cannot, however, be the origin of the recovery effect, which arises in the FPS of Ly-α forests that are strongly dominated by absorption such as in figure 4.1. Our hypothesis of the origin of the recovery effect is based on a visual inspection of spectra like figure 4.1, and especially the frequency range around $v_f \approx 1750\,\mathrm{km\,s^{-1}}$. Here, we see that the Ly-α forest calculated while accounting for peculiar velocities displays more small-scale oscillations than the Ly-α forest calculated without peculiar velocities. This happens because peculiar velocities tend to be directed away from voids; the optical depth caused by matter in these voids is thus shifted outside of the frequency range corresponding to their spatial size. Hence, a small section of the void may become responsible for the transmission pattern of a sizeable part of the Ly-α forest and most structures in this small section may become visible, no longer obscured by thermal broadening from denser regions. The additional small scale structure thus revealed would then be responsible for the recovery effect. Testing this hypothesis will require further research.

Version of July 8, 2022– Created July 8, 2022 - 21:51

Finally, we have attempted to describe $\mathcal{D}$ in terms of a Gaussian cutoff because we could motivate such a model through an analogy with pressure effects described by (2.53). In figure 4.2, the deviation from such a Gaussian cutoff for $0.08\,\mathrm{s\,km^{-1}} \lesssim k_v \lesssim 0.1\,\mathrm{s\,km^{-1}}$ was then interpreted as being due to the onset of the recovery effect. We cannot, however, be certain that this interpretation is correct without a description of the recovery effect: this deviation might equally well indicate that $\mathcal{D}$ cuts off less rapidly than a Gaussian cutoff, for example exponentially. We did not consider such an option since we could not physically motivate it and a Gaussian cutoff was clearly acceptable, but further investigation is needed to see if there is an even more successful way of describing $\mathcal{D}$.

6.2 The redshift dependence of the fitted parameters

As (3.43) works reasonably well for $4.0 \leq z \leq 5.5$, the redshift dependence of A and B as presented in section 5.7 becomes relevant. Section 5.7 claimed that a constant value of A could be rejected, while this could not be done for B. This is mildly surprising, as B should depend on for example the difference between $\langle n_H^2 \rangle$ and $\langle n_H \rangle^2$, which is a factor $\langle (1+\delta_H)^2 \rangle$. Furthermore, B should also depend on the difference between $\langle \alpha_{\mathrm{HII}}(T) \rangle$ and $\alpha_{\mathrm{HII}}(T_0)$; since approximately $\alpha_{\mathrm{HII}}(T) \propto T^{-0.7}$, and the temperature is set by the density through (3.7), this would introduce a factor of approximately $\langle (1+\delta_H)^{0.7(1-\gamma)} \rangle$. These factors do not cancel in general, and hence we would expect B to evolve as the density contrast develops over time. Indeed, the fact that a constant B cannot be ruled out does not imply that B truly is constant, only that the currently available data is not necessarily inconsistent with a constant B.
In contrast to B, a constant A can already be ruled out by the results presented here. Considering figure 5.12a, A could evolve non-monotonically with a general trend of increase over time. However, until a convincing model is formulated for the redshift dependence of A and B, we must treat them as purely phenomenological parameters.

6.3 The importance of the peculiar velocity cutoff

Astronomers are acutely aware of the distortions to the density field in 'redshift space' (i.e. with distances estimated directly from the redshift) with respect to the density field in 'real space' due to peculiar velocities.These distortions have typically been modelled as inducing a certain amount of bias [13]. There have been studies dedicated to quantifying the influence of peculiar velocities on statistics used to describe the LSS (e.g. [48] or [49]); indeed, many observational surveys of the LSS explicitly note how they approach the distortions introduced by peculiar velocities [17, 32, 33], although sometimes the main results are also simply presented in redshift space [50] or peculiar velocities are rendered irrelevant by smoothing the Ly-α forest to a sufficiently high degree [18]. This serves to illustrate that disentangling the effects of peculiar velocities from those of thermal or pressure broadening and the underlying matter distribution is an extremely important issue in observational cosmology.
We note that [48] also found that the non-linear one-dimensional power spectrum cuts off faster in redshift space than in real space, similarly to the effect we noted here. However, they remark that this effect strongly depends on the precise form of the fil-

Version of July 8, 2022– Created July 8, 2022 - 21:51

tering function introduced by peculiar velocities. Here, we have shown that often, this cutoff is well-modelled by a Gaussian. [48] also does not mention the recovery effect. We are not aware of earlier work that has explicitly attempted to describe the influence of peculiar velocities at these high redshifts as a Gaussian cutoff in the FPS, but such a cutoff may be relevant as it mainly affects the FPS on scales that are regularly probed with current observations of the Ly-α forest [47]. Furthermore, it depends on the thermal state of the IGM, which is relatively poorly constrained. This translates into an uncertainty in the scale on which the cutoff due to thermal broadening occurs, but as we have shown here, it should also translate into an uncertainty on the scale on which the cutoff due to peculiar velocities occurs. Indeed, we would expect uncertainties in the photo-ionisation rate to influence the FPS not only through the thermal broadening scale, but also through the peculiar velocity cutoff scale.
However, we should not overestimate the importance of this Gaussian cutoff either. In the high k_v-range, the influence of peculiar velocities on the FPS can no longer be described as a Gaussian, but is instead dominated by the recovery effect, for which we have suggested a hypothesis of its origin but no (phenomenological) model.

6.4 Outlook and further research

The research presented in this thesis can be extended in several aspects. The most obvious one is the recovery effect, which dominates the impact of peculiar velocities at small scales yet has mostly been ignored so far. A model of this effect could allow a more accurate extraction of Δv from $\mathcal{D}$, either because it would allow for a correction for the recovery effect (thus isolating the Gaussian cutoff) or because Δv as predicted by (3.43) might be a characteristic scale for the recovery effect as well. It may also allow for a more robust answer to the issue of whether (4.5) is truly the best description of $\mathcal{D}$ on small k_v. However, a complete model need not be necessary, if a more sophisticated procedure could be constructed for selecting the range of k_v to be used to fit (4.5).
As we mentioned, failure of our procedure to select the optimal range of k_v to fit (4.5) may have been responsible for the overly high Δv at high temperatures in figure 5.7b, and possibly for other deviations from (3.43) such as the sudden changes in Δv as a function of thermal broadening as well. Correctly determining the optimal range of k_v for fitting (4.5) could thus allow us to more accurately determine whether or not Δv is indeed independent of thermal broadening.
Finally, a more accurate model is certainly needed for the dependence of Δv on σ_u. (3.43) saw considerable success in predicting the average ratio $\frac{\Delta v}{\sigma_u}$ (at worst, the realised average and the prediction of (3.43) differed 1.6σ), but it was never an acceptable model for the true dependence of Δv on σ_u, in which Δv gradually varies around the predicted direct proportionality. A more accurate model might allow us to constrain A and B and their redshift evolution more tightly than we have done so far.
The most obvious application of our interpretation of Δv as defined in (3.43) as a cutoff scale in a Gaussian cutoff in the FPS is that it allows us to distinguish suppression in the FPS due to peculiar velocities from suppression due to thermal broadening, pressure broadening and warm dark matter free streaming. Since (3.43) does indeed seem to correctly describe Δv at a considerable range of redshifts, more accurate knowledge of the thermal and dynamical state of the IGM will thus allow us to further isolate the effect of free streaming, and thus constrain models of dark matter.

Version of July 8, 2022– Created July 8, 2022 - 21:51

6.5 Summary

1. In this thesis, we gave a brief overview of the physics and mathematics used to describe the structure and evolution of the large-scale structure of the universe.
2. Subsequently, we introduced a description of the ionisation state of the intergalactic medium and derived an expression of its optical depth to Ly-α radiation.
3. We proposed the following model as a description of the scale on which peculiar velocities impact the Ly-α forest:

$$\Delta v = A\sigma_u \sqrt{2 \ln \left(B \frac{\langle n_H \rangle^2}{n_0(z_{\mathrm{LOS}})} \frac{\alpha_{\mathrm{HII}}(T_0)}{\Gamma_{\mathrm{HI}}} \right)}, \tag{6.1}$$

   With σ_u the dispersion in the peculiar velocities, $\langle n_H \rangle$ the average total hydrogen density, z_{LOS} the redshift of the line of sight, α_{HII} the recombination rate, T_0 the temperature amplitude used in (3.7) and Γ_{HI} the photo-ionisation rate. $n_0 = \frac{H(z_{\mathrm{LOS}})}{\sigma_0 \lambda_\alpha}$ with H the Hubble parameter, σ_0 the amplitude of the Ly-α absorption cross section and λ_α the Ly-α wavelength is a reference density.
4. Furthermore, we proposed that this scale could be interpreted as the spatial scale on which peculiar velocities introduce a Gaussian cutoff to the flux power spectrum of the Ly-α forest, as long as this Ly-α forest is dominated by absorption and hence only has a few transmission features.
5. We then tested these models ((6.1) and the Gaussian cutoff model) to the flux power spectrum as calculated from high-resolution hydrodynamical simulations for a considerable range of densities $\langle n_H \rangle$, temperatures T_0, peculiar velocity dispersions and amounts of thermal broadening at redshifts $4.0 \leq z \leq 6.0$. These tests indicate that a Gaussian cutoff is indeed often an acceptable description of the influence of peculiar velocities at low k_v.
6. They also indicated that the dependence on density and temperature of the cutoff scale associated with this cutoff could indeed be described relatively well by (6.1) at redshifts $z \leq 5.5$. At redshift $z = 6.0$, (6.1) could not be acceptably fitted to the realised Δv.
7. Our tests also indicated that while (6.1) could correctly predict the average ratio $\frac{\Delta v}{\sigma_u}$, it failed to correctly reproduce the exact dependence of Δv on σ_u. The prediction of (6.1) that Δv should be independent of thermal broadening cannot be rejected at any of the redshifts considered here.
8. Finally, we considered the redshift dependence of A and B. A appears to significantly vary with redshift in a non-monotonic way, while we cannot at present exclude the possibility that B is constant with redshift, although we consider this to be a consequence of the limited information we currently have on B.
9. The main venue in which the research presented here can be extended is through a more accurate description of the recovery effect, a phenomenon in which peculiar velocities cause the flux power spectrum to acquire more power on small scales, which forms the main limitation to the Gaussian cutoff model. Such a description should yield more accurate determinations of Δv and provide more

Version of July 8, 2022– Created July 8, 2022 - 21:51

insight into the matter of the independence of Δv from thermal broadening or the possibility of the cutoff being of another form than Gaussian.

10. Another way in which (6.1) can be extended is through a more sophisticated treatment of the dependence of Δv on σ_u, which could possibly constrain the values of A and B even further.

The model proposed in (6.1) may serve to constrain the cutoff scale induced by peculiar velocities. If this can be combined with cutoff scales due to thermal and pressure broadening, the small scale suppression due to free streaming may be isolated, and hence be used to constrain models of dark matter.

Acknowledgements

We would like to extend our gratitude to Ivan Ridkokasha and Kyrylo Bondarenko, for their guidance, useful discussions, and helpful comments. Furthermore, we thank Alexey Boyarsky, who brought us all into contact and in general initiated this project. Finally, our gratitude goes out to Matthieu Schaller for his interesting questions and organisational aid.

Bibliography

[1] Y. Sofue, Y. Tutui, M. Honma, A. Tomita, T. Takamiya, J. Koda, and Y. Takeda. Central Rotation Curves of Spiral Galaxies. *The Astrophysical Journal*, 523:136–146, Sep 1999.

[2] S. De Rijcke, P. Prugniel, F. Simien, and H. Dejonghe. The internal dynamics of the Local Group dwarf elliptical galaxies NGC 147, 185 and 205. *Monthly Notices of the Royal Astronomical Society*, 369:1321–1333, Mar 2006.

[3] J. S. Mulchaey, D. S. Davis, R. F. Mushotzky, and D. Burstein. Diffuse X-ray emission from the NGC 2300 group of galaxies - Implications for dark matter and galaxy evolution in small groups. *The Astrophysical Journal*, 404:L9–L12, Feb 1993.

[4] D. Clowe, A. Gonzalez, and M. Markevitch. Weak-Lensing Mass Reconstruction of the Interacting Cluster 1E 0657-558: Direct Evidence for the Existence of Dark Matter. *The Astrophysical Journal*, 604:596–603, Apr 2004.

[5] G. F. Chapline. Cosmological effects of primordial black holes. *Nature*, 253:251–252, Jan 1975.

[6] S. Dodelson and L. M. Widrow. Sterile neutrinos as dark matter. *Physical Review Letters*, 72:17–20, Jan 1994.

[7] M. R. Lovell, S. Bose, A. Boyarsky, S. Cole, C. S. Frenk, V. Gonzalez-Perez, R. Kennedy, O. Ruchayskiy, and A. Smith. Satellite galaxies in semi-analytic models of galaxy formation with sterile neutrino dark matter. *Monthly Notices of the Royal Astronomical Society*, 461:60–72, Jun 2016.

[8] M. Milgrom. A modification of the Newtonian dynamics as a possible alternative to the hidden mass hypothesis. *The Astrophysical Journal*, 270:365–370, Jul 1983.

[9] D. Paraficz, J. P. Kneib, J. Richard, A. Morandi, M. Limousin, E. Jullo, and J. Martinez. The Bullet cluster at its best: weighing stars, gas, and dark matter. *Astronomy & Astrophysics*, 594:A121, Oct 2016.

[10] T. D. Brandt. Constraints on MACHO dark matter from compact stellar systems in ultra-faint dwarf galaxies. *The Astrophysical Journal*, 824:L31, Jun 2016.

[11] N. Aghanim, Y. Akrami, M. Ashdown, J. Aumont, C. Baccigalupi, M. Ballardini, A. J. Banday, R. B. Barreiro, N. Bartolo, S. Basak, R. Battye, K. Benabed, J. P. Bernard, M. Bersanelli, P. Bielewicz, J. J. Bock, J. R. Bond, J. Borrill, F. R. Bouchet, ..., and A. Zonca. Planck 2018 results: VI. Cosmological parameters. *Astronomy & Astrophysics*, 641, Sep 2020.

[12] A. Boyarsky, J. Lesgourgues, O. Ruchayskiy, and M. Viel. Lyman-α constraints on warm and on warm-plus-cold dark matter models. *Journal of Cosmology and Astroparticle Physics*, 2009:012, May 2009.

[13] Peacock, J.A. *Cosmological Physics*. Cambridge University Press, Cambridge, 1998. 1st ed.

[14] Sparke, L. S. and Gallagher, J. S., III. *Galaxies in the Universe*. Cambridge University Press, Cambridge, 2007. 2nd ed.

[15] W. L. W. Sargent, P. J. Young, A. Boksenberg, and D. Tytler. The distribution of Lyman-alpha absorption lines in the spectra of six QSOs - Evidence for an intergalactic origin. *The Astrophysical Journal Supplement Series*, 42:41–81, Jan 1980.

[16] V. Iršič, M. Viel, T. A. M. Berg, V. D'Odorico, M. G. Haehnelt, S. Cristiani, G. Cupani, T. S. Kim, S. López, S. Ellison, G. D. Becker, L. Christensen, K. D. Denney, G. Worseck, and J. S. Bolton. The Lyman-alpha forest power spectrum from the XQ-100 Legacy Survey. *Monthly Notices of the Royal Astronomical Society*, 466:4332–4345, May 2016.

[17] F. S. Kitaura, S. Gallerani, and A. Ferrara. Multiscale inference of matter fields and baryon acoustic oscillations from the Lyα forest. *Monthly Notices of the Royal Astronomical Society*, 420:61–74, Jan 2012.

[18] H. Zhan and L. Fang. The Large-Scale rms Bulk Velocity Estimated from Quasar Lyα Forests. *The Astrophysical Journal*, 566:9–14, Feb 2002.

[19] A. Garzilli, A. Boyarsky, and O. Ruchayskiy. Cutoff in the Lyman-α forest power spectrum: Warm IGM or warm dark matter? *Physics Letters B*, 773:258–264, Oct 2017.

[20] A. Garzilli, T. Theuns, and J. Schaye. The broadening of Lyman-α forest absorption lines. *Monthly Notices of the Royal Astronomical Society*, 450:1465–1476, Feb 2015.

[21] A. Garzilli, A. Magalich, T. Theuns, C. S. Frenk, C. Weniger, O. Ruchayskiy, and A. Boyarsky. The Lyman-α forest as a diagnostic of the nature of the dark matter. *Monthly Notices of the Royal Astronomical Society*, 489:3456–3471, Aug 2019.

[22] Gorbunov, D. S. and Rubakov, V. A. *Introduction to the Theory of the Early Universe: Cosmological Perturbations and Inflationary Theory*. World Scientific Publishing, London, 2011.

[23] Mo, H. and Van den Bosch, F. and White, S. *Galaxy Formation and Evolution*. Cambridge University Press, Cambridge, 2010.

[24] Hartle, J. B. *Gravity: An Introduction to Einstein's General Relativity*. Pearson, Harlow, 2014. First Edition.

[25] Bergström, L., and Goobar, A. *Cosmology and Particle Astrophysics*. Springer Publishing, 2007. 2nd ed.

[26] H. Yu and F. Y. Wang. New model-independent method to test the curvature of the universe. *The Astrophysical Journal*, 828, Sep 2016.

[27] K. C. Wong, S. H. Suyu, G. C. F. Chen, C. E. Rusu, M. Millon, D. Sluse, V. Bonvin, C. D. Fassnacht, S. Taubenberger, M. W. Auger, S. Birrer, J. H. H. Chan, F. Courbin, S. Hilbert, O. Tihhonova, T. Treu, A. Agnello, X. Ding, I. Jee, . . ., and G. Meylan. H0LiCOW - XIII. A 2.4 per cent measurement of H0 from lensed quasars: 5.3σ tension between early- and late-Universe probes. *Monthly Notices of the Royal Astronomical Society*, 498:1420–1439, Sep 2019.

[28] A. Friedman. On the Curvature of Space. *General Relativity and Gravitation*, 31:1991–2000, Dec 1999.

[29] A. G. Riess, A. V. Filippenko, P. Challis, A. Clocchiatti, A. Diercks, P. M. Garnavich, R. L. Gilliland, C. J. Hogan, S. Jha, R. P. Kirshner, B. Leibundgut, M. M. Phillips, D. Reiss, B. P. Schmidt, R. A. Schommer, R. C. Smith, J. Spyromilio, C. Stubbs, N. B. Suntzeff, and J. Tonry. Observational Evidence from Supernovae for an Accelerating Universe and a Cosmological Constant. *The Astronomical Journal*, 116:1009–1038, Sep 1998.

[30] D. J. Fixsen. The temperature of the Cosmic Microwave Background. *The Astrophysical Journal*, 707:916–920, Nov 2009.

[31] A. Doroshkevich, D. L. Tucker, S. Allam, and M. J. Way. Large scale structure in the SDSS galaxy survey. *Astronomy & Astrophysics*, 418:7–23, Apr 2004.

[32] A. Zandivarez, M. E. Merchán, and N. D. Padilla. Galaxy groups in the 2dF Galaxy Redshift Survey: large-scale structure with groups. *Monthly Notices of the Royal Astronomical Society*, 344:247–256, Sep 2003.

[33] E. Hawkins, S. Maddox, S. Cole, O. Lahav, D. S. Madgwick, P. Norberg, J. A. Peacock, I. K. Baldry, C. M. Baugh, J. Bland-Hawthorn, T. Bridges, R. Cannon, M. Colless, C. Collins, W. Couch, G. Dalton, R. De Propris, S. P. Driver, G. Efstathiou, . . ., and K. Taylor. The 2dF Galaxy Redshift Survey: correlation functions, peculiar velocities and the matter density of the Universe. *Monthly Notices of the Royal Astronomical Society*, 346:78–96, Nov 2003.

[34] J. R. Bond, L. Kofman, and D. Pogosyan. How filaments of galaxies are woven into the cosmic web. *Nature*, 380:603–606, Apr 1996.

[35] N. Y. Gnedin and L. Hui. Probing the Universe with the Ly forest – I. Hydrodynamics of the low-density intergalactic medium. *Monthly Notices of the Royal Astronomical Society*, 296:44–55, May 1998.

[36] A. Magalich. *Probing the properties of dark matter particles with astrophysical observations*. Doctoral thesis, Leiden University, Dec 2019. https://scholarlypublications.universiteitleiden.nl/handle/1887/82071.

[37] R. A. Simcoe. High-Redshift Intergalactic CIV Abundance Measurements from the Near-Infrared Spectra of Two z $\sim$ 6 QSOs. *The Astrophysical Journal*, 653:977–987, Sep 2006.

[38] J. X. Prochaska, H. Chen, J. C. Howk, B. J. Weiner, and J. Mulchaey. Probing the Intergalactic Medium-Galaxy Connection toward PKS 0405-123. I. Ultraviolet Spectroscopy and Metal-Line Systems. *The Astrophysical Journal*, 617:718–745, Aug 2004.

[39] J. Oñorbe, J. F. Hennawi, and Z. Lukić. Self-consistent Modeling of Reionization in Cosmological Hydrodynamical Simulations. *The Astrophysical Journal*, 837:106–131, Mar 2017.

[40] J. E. Gunn and B. A. Peterson. On the Density of Neutral Hydrogen in Intergalactic Space. *The Astrophysical Journal*, 142:1633–1636, Nov 1965.

[41] R. H. Becker, X. Fan, R. L. White, M. A. Strauss, V. K. Narayanan, R. H. Lupton, J. E. Gunn, J. Annis, N. A. Bahcall, J. Brinkmann, A. J. Connolly, I. Csabai, P. C. Czarapata, M. Doi, T. M. Heckman, G. S. Hennessy, E. Ivezić, G. R. Knapp, D. Q. Lamb, . . ., and D. G. York. Evidence for Reionization at z $\sim$ 6: Detection of a Gunn-Peterson Trough in a z = 6.28 Quasar. *The Astronomical Journal*, 122:2850–2857, Sep 2001.

[42] Rybicki, G. B. and Lightman, A. P. *Radiative Processes in Astrophysics*. Wiley-VHC, Weinheim, 1991.

[43] L. Hui and N. Y. Gnedin. Equation of state of the photoionized intergalactic medium. *Monthly Notices of the Royal Astronomical Society*, 292:27–42, Nov 1997.

[44] T. Theuns, A. Chalk, M. Schaller, and P. Gonnet. SWIFT: task-based hydrodynamics and gravity for cosmological simulations. *ArXiv e-prints*, Aug 2015.

[45] V. Springel. Smoothed Particle Hydrodynamics in Astrophysics. *Annual Review of Astronomy and Astrophysics*, 48:391–430, Aug 2010.

[46] T. Hsyu, R. J. Cooke, J. X. Prochaska, and M. Bolte. The PHLEK Survey: A New Determination of the Primordial Helium Abundance. *The Astrophysical Journal*, 896:77–103, Jun 2020.

[47] N. G. Karaçayli, N. Padmanabhan, A. Font-Ribera, V. Iršič, M. Walther, D. Brooks, E. Gaztañaga, R. Kehoe, M. Levi, P. Ntelis, N. Palanque-Delabrouille, and G. Tarlé. Optimal 1D Ly-α Forest Power Spectrum Estimation – II. KODIAQ, SQUAD & XQ-100. *Monthly Notices of the Royal Astronomical Society*, 509:2842–2855, Nov 2021.

[48] V. Desjacques and A. Nusser. Redshift distortions in one-dimensional power spectra. *Monthly Notices of the Royal Astronomical Society*, 351:1395–1400, Jul 2004.

[49] A. Jiang, W. Liu, W. Fang, and W. Zhao. Effects of peculiar velocities on the morphological properties of large-scale structure. *Physical Review D*, 105:103028, May 2022.

[50] S. Maitra, R. Srianand, and P. Gaikwad. Measurement of redshift-space two- and three-point correlation of Lyα absorbers at $1.7 < z < 3.5$: implications on evolution of the physical properties of IGM. *Monthly Notices of the Royal Astronomical Society*, 509:1536–1556, Jan 2022.

Appendix A

Comparing simulations to observations

To verify that our calculation of the flux power spectrum (FPS) yields reasonable results, the FPS was determined at redshifts $z = 4.0$ and $z = 4.4$ using the standard simulation parameters, i.e. T_0 and γ as simulated and n_H as calculated using (4.1). This FPS was then compared to data from [47]. This comparison is shown in figure A.1; in general, the simulations match the observations relatively well. The deviation at $z = 4.0$ is more significant at small scales, perhaps because the `SWIFT` simulations used a slightly too warm thermal history as compared to the true thermal history. In general, the maximum difference between the observed and simulated FPS amounted to 4.6σ at $z = 4.0$ and 1.5σ at $z = 4.4$; ignoring the two observations at $k_v \geq 0.079\,\mathrm{s\,km^{-1}}$, which may differ because of the different thermal histories, the maximum difference at $z = 4.0$ is 2.7σ. We thus conclude that our calculations do indeed produce reasonable estimates for the FPS.

Version of July 8, 2022– Created July 8, 2022 - 21:51

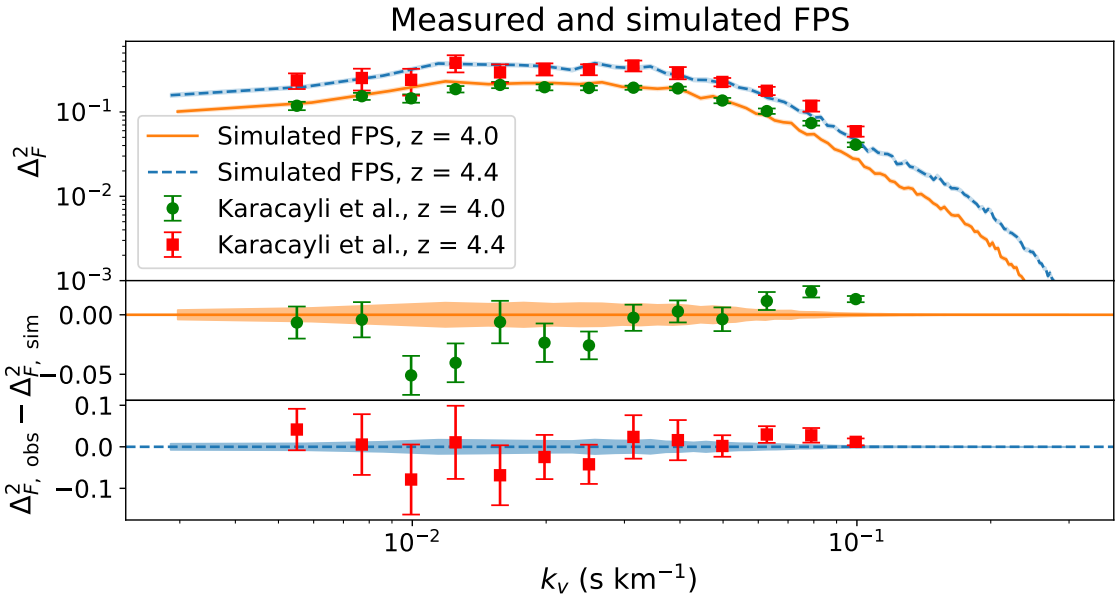

Figure A.1: *A comparison between the FPS obtained from the* `SWIFT` *simulation and from observations. The solid orange curve and dashed blue curve show the FPS calculated from the simulation at $z = 4.0$ and $z = 4.4$ respectively; error margins are shown as shaded regions in the respective colours. The green circles and red squares present the FPS from [47] measured at $z = 4.0$ and $z = 4.4$ respectively. The upper frame directly shows all FPS, whereas the lower two panels demonstrate the difference between the observed and simulated FPS at $z = 4.0$ and $z = 4.4$ respectively; in general the deviation is not extremely significant.*

Version of July 8, 2022– Created July 8, 2022 - 21:51

Appendix B

Checking the effects of finite resolution

To verify that the impact seen in figure 4.2 is not a numerical artefact, we calculated $\mathcal{D}$ using a simulation with artificially lowered resolution. This lower resolution was achieved by replacing each subsequent pair of data points on the density contrast and peculiar velocity along the line of sight (LOS) by their average. This way, we effectively obtained the data along an LOS as it would have been produced by a simulation of half the resolution achieved in the actual simulation. Any effect mainly due to a numerical artefact as a consequence of the finite simulation resolution should respond strongly to this considerable change in resolution.
Figure B.1 shows the difference between $\mathcal{D}$ as calculated with the regular simulations used in this thesis ('high resolution') and as calculated with the lowered resolution ('low resolution') at three different redshifts. This difference is never significant by any measure; indeed, the largest deviation at a given redshift never exceeds the minimum error on any deviation at the same redshift, even though these do not have to occur at the same k_v. We conclude that there is no indication that the effects treated in this thesis are numerical artefacts.

Version of July 8, 2022– Created July 8, 2022 - 21:51

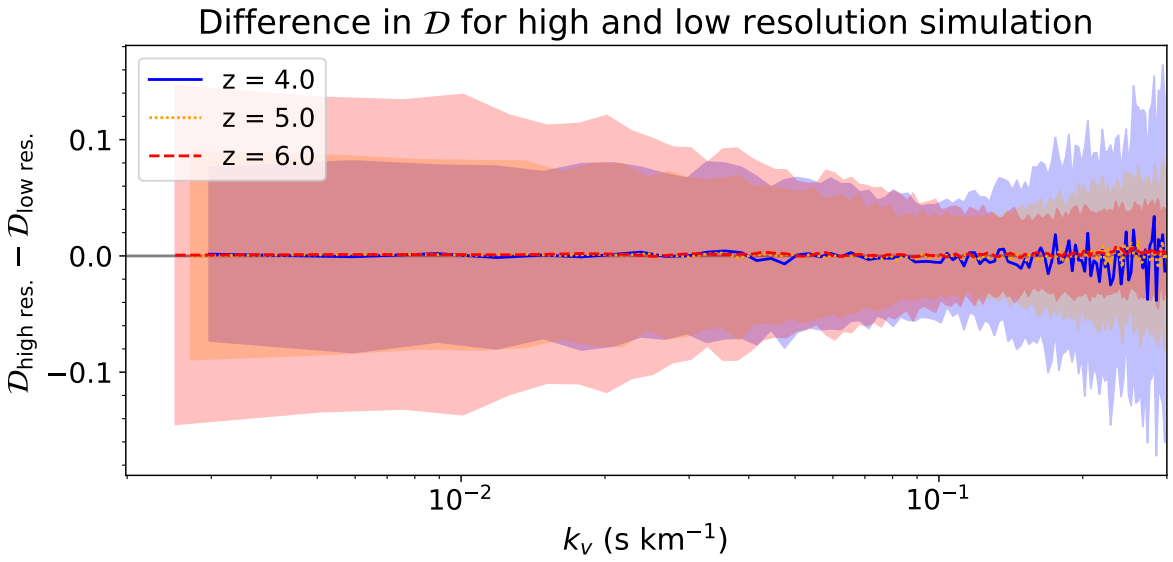

Figure B.1: *The difference between $\mathcal{D}$ as defined in (4.4) calculated while using a high-resolution simulation (i.e. the resolution of the actual simulations used in this thesis) and using a simulation in which the resolution was artificially lowered by taking the average of subsequent data points along all LOS. The solid blue line shows this difference at $z = 4.0$, the dotted orange line shows the difference at $z = 5.0$ and the dashed red line shows the difference at $z = 6.0$; the shaded regions show the error margins on these differences, and have the same colour as the corresponding curve. Note that no curve leaves the range defined by the error margins; the differences are never significant.*